Meteorol. Atmos. Phys. 54, 3–27 (1994)

Meteorology and Atmospheric Physics



551.551.8

[1] Department of Electrical Engineering, Colorado State University, Fort Collins, Colorado, U.S.A.
[2] National Center for Atmospheric Research, Research Applications Program, Boulder, Colorado, U.S.A.
[3] Dipartimento di Ingegneria Elettronica, Università di Roma "La Sapienza", Rome, Italy
[4] National Aeronautics and Space Administration, ES-43, Marshall Space Flight Center, Alabama, U.S.A.
[5] Universities Space Research Association, NASA/Marshall Space Flight Center, Huntsville, Alabama, U.S.A.

# Active and Passive Microwave Remote Sensing of Precipitating Storms During CaPE. Part I: Advanced Microwave Precipitation Radiometer and Polarimetric Radar Measurements and Models

**J. Turk[1], J. Vivekanandan[2], F. S. Marzano[3], R. E. Hood[4], R. W. Spencer[4], and F. J. LaFontaine[5]**

With 16 Figures

Received March 3, 1993
Revised August 11, 1993

**Summary**

The Advanced Microwave Precipitation Radiometer (AMPR), an across-track scanning, four-channel (10.7, 19.35, 37.1, 85.5 GHz) total-power radiometer system, was instrumented aboard a NASA ER-2 aircraft during the 1991 CaPE (Convection and Precipitation/Electrification) project in central Florida. At a 20 km flight altitude, the AMPR provides fine-scale microwave imagery of Earth surfaces and its atmosphere, and is well-suited for diverse hydrological applications. During overflights of precipitation, coincident ground-based radar measurements were taken with the NCAR CP-2 dual-frequency, dual-polarization radar system. After remapping the radar data into a format compatible with the AMPR scanning geometry, the radar-derived profiles of rain, melting, and frozen hydrometeors are compared against the AMPR equivalent blackbody brightness temperature ($T_B$) imagery. Microwave radiative transfer modeling procedures incorporating the radar-derived hydrometeor profiles were used to simulate the multifrequency AMPR imagery over both land and ocean background ER-2 flights. Within storm cores over land, columnar ice water paths up to 20 kg m$^{-2}$ gradually depressed the 85 GHz $T_B$ as low as 100 K. The presence of tall vertical reflectivity columns encompassing $>20$ kg m$^{-2}$ columnar ice water path often produced 37 GHz $T_B < 85$ GHz $T_B$ directly over the core. Over ocean, the 10 GHz channel provided the clearest correlation with the rainfall amounts, whereas the 19 GHz channel saturated near 260 K past 10–15 mm hr$^{-1}$ rain rate as determined by radar. Scattering by ice and melting ice at 37 GHz produced $T_B$ ambiguities over both raining and clear-ocean regions. Sensitivity to the columnar mixed phase region via the intermediate frequencies (19 and 37 GHz) is demonstrated and explained with the radar-derived $T_B$ modeling. By superimposing vertical profiles of cloud liquid water (which this radar cannot measure) upon the radar-inferred hydrometeor structure, additional information on the location of the peak cloud water and its amount relative to the vertical ice structure can be noted, along with a possible inference of the dominant ice particle size within the upper storm core.

These results suggest that as the resolution of passive radiometric measurements approaches dimensions where the antenna beams become increasingly filled by the cloud, precipitation retrieval via multifrequency $T_B$ input is well-suited to a vertical profiling-type algorithm. This is further examined in Part II of this manuscript, where the radar-derived vertical hydrometeor profiles are used to test the applicability of a multispectral cloud model-based approach to passive microwave precipitation retrieval from space.

## I. Introduction

Spaceborne remote sensing satellites employing combinations of active and passive microwave sensors are planned to meet the need for reliable

estimates of rainfall and liquid and ice water content. Noteworthy instruments include the Tropical Rainfall Measuring Mission (TRMM) satellite, carrying the TRMM Microwave Imager (TMI) as well as a 14 GHz radar, and the European Space Agency's Multifrequency Imaging Microwave Radiometer (MIMR). The current series of DMSP Special Sensor Microwave Imager (SSM/I) sun-synchronous satellite radiometers have proven the applicability of microwave channels between 19 and 85 GHz in measurements of the surface and atmospheric parameters which drive the Earth's hydrological cycle. In addition to precipitation, these parameters include sea surface temperature, sea ice, water vapor, cloud water, snow cover and soil moisture. For the SSM/I, the on-Earth resolution varies from 16 × 14 km at 85.5 GHz to 70 × 45 km at 19.35 GHz, where in most instances, the latter is considerably greater than the dimensions of typical mid-latitude or tropical precipitating cloud systems. Since the antenna beamwidth can be filled with a mixture of precipitating and non-precipitating cloud as well as the underlying surface, the footprint-averaged rain rates determined by multispectral $T_B$ observations will vary widely. This tendency is well-recognized and several techniques have been developed for mitigation (Prabhakara et al., 1992; Grody, 1991; Liu and Curry, 1992). Radiometers such as TMI will provide resolutions ranging from 37 km at 10 GHz to 5 km at 90 GHz. As a result, the multifrequency $T_B$ response from satellite radiometers will vary quite differently as the instrument spatial resolution begins to approach the dimensions at which rainfall is generated in typical cloud bands, and precipitation retrieval techniques developed with SSM/I-sized measurements may not be applicable or require modification.

With their lower altitude observational platform, airborne passive microwave radiometric measurements can be made at a much finer scale than their spaceborne counterparts. In particular, the NASA ER-2 research aircraft fleet, with their 20 km flight altitude, are ideal for remote measurements over the tallest thunderstorms. Hakkarinen and Adler (1988) analyzed 92 and 183 GHz imagery from the airborne Advanced Microwave Moisture Sounder (AMMS) and compared the results with ground-based radar imagery. Regions of $T_B$ depressions over precipitation showed agreement with the radar reflectivity at heights of 6 to 7 km.

In 1986, the Cooperative Huntsville Meteorological Experiment (COHMEX) provided the opportunity to gather ER-2 passive radiometric measurements over precipitating clouds at 18, 37, 92, and 183 GHz along with support from the National Center for Atmospheric Research (NCAR) CP-2 multiparameter radar. Fulton and Heymsfield (1991) analyzed several flight lines and tied the evolution of the CP-2 dual frequency ratio hail signal (DFR-HS), linear depolarization ratio (LDR), and differential reflectivity $Z_{DR}$ to the corresponding multifrequency $T_B$ features. Vivekanandan et al. (1990) attempted to reproduce the multifrequency $T_B$ over the core region using simple radar-derived vertical microphysical profiles of rain, melting, and ice hydrometeors in a radiative transfer model. Kummerow et al. (1991) employed the COHMEX $T_B$ data in a statistical regression procedure which reconstructs a multilayered vertical hydrometeor profile. The two part series by Adler et al. (1990) and Yeh et al. (1990) used reflectivity-mass content relationships to derive rain and ice profiles, and compared the results of a microwave radiative transfer model with the COHMEX $T_B$ data. Mugnai et al. (1990) performed a cloud model simulation from a COHMEX storm and used the results to model the radiometric behavior at SSM/I frequencies.

In retrospect, one difficulty associated with the COHMEX data interpretation was due to differences in the radiometer viewing. The 18 and 37 GHz measurements were taken in a 45° ahead non-scanning stare mode along the flight track, while the 92 and 183 GHz measurements were taken with the AMMS in an across-track scanning mode. Hence, the low frequency channels viewed the cloud along a slant path at an earlier time than the higher frequency channels. Most investigators chose to apply a temporal offset to the data to align the 37 and 92 GHz $T_B$ minima over the store core, but the differing view angle still remained. Nonetheless, many important discoveries relating the radar observables to the fine-scale $T_B$ observations were gained for the first time.

The following measurements and modeling employ a relatively new instrument, the Advanced Microwave Precipitation Radiometer (AMPR), designed and built to meet the specifications provided by the NASA Marshall Space Flight Center (MSFC) (Spencer et al., 1993). At AMPR resolutions, the radiometric behavior of precipitating cloud structures is quite different than that

associated with larger SSM/I-sized resolutions. The AMPR is specifically designed to mount aboard an ER-2 and operates four channels between 10 and 85 GHz. Upwelling scene emission is directed at a common rotating reflector for all four channels in an across-track scanning operation. The 10 GHz channel is especially useful for observing moderately high precipitation over the ocean, under which conditions a 19 GHz channel may saturate or begin to exhibit scattering effects. During October 1990, engineering test flights were taken over the Gulf of Mexico, which have been reported by Smith et al. (1993). Their results demonstrated marked improvement in a precipitation retrieval algorithm over ocean by comparing retrieval results with and without the inclusion of the 10 GHz channel. In summer 1991, first flights during a field experiment were realized during the Convection and Precipitation/Electrification (CaPE) experiment near Kennedy Space Center, Florida, with the NCAR CP-2 radar again providing multiparameter radar support. Within the realm of polarimetric radar remote sensing of precipitation, one attempts to retrieve information regarding the water phase, location, and content, the associated distributions of the particle size, and to a certain extent, the particle shape and orientation. For applications related to radiative transfer, it is mainly the drop size distribution (DSD) of the rain and ice particles that controls the overall emitted, absorbed, and scattered radiation. Development of fast-switching dual polarization radar systems have enabled the measurement of additional independent radar parameters, such as differential reflectivity $Z_{DR}$ and differential propagation phase $\phi_{DP}$ which, for example, have potential to estimate parameters describing a modified gamma size distribution of rain drops (Sachidananda and Zrnic, 1986; Balakrishnan and Zrnic, 1990). However, extensions to frozen precipitation amounts are not yet fully understood. Polarimetric studies might be relevant in pristine crystals which exhibit differential scattering characteristics, but hail, graupel, and low density snow particles display little polarimetric dependent signatures at common weather radar wavelengths.

It is not difficult to envisage situations where there are various mixtures of rain, hail, cloud water, and melting occupying volumes comparable to typical pulsed Doppler radar resolution volumes ($\approx 1\,\text{km}^3$). While the mixed phase region above and below the 0 °C isotherm level provides the most telltale signature of the overall storm state (growth and decay, overall intensity), it is very difficult to apportion polarimetric radar measurements into individual contributions from different categories. Measurements of the linear or circular depolarization ratio are useful for identifying regions of wet growth (such as an active, growing cell undergoing a transformation from suspended supercooled rain into a glaciated state) or steady decay and melting (the stratiform bright band) (Herzegh and Jameson, 1992), but at present, few attempts have been made to incorporate depolarization measurements in a quantitative fashion. Vivekanandan et al. (1992) have investigated the polarimetric behavior of mixtures of rain and hail using a technique which combines the individual Mueller matrix describing each category in the mixture.

This two part paper couples the efforts of several research groups in the United States and Italy in a thorough analysis of the CaPE measurements from 12 August 1991, including radar microphysical retrievals, combined radar-radiative transfer modeling, and the application of a multispectral, cloud model-based precipitation retrieval algorithm to the AMPR measurements. In this Part I section, research has been directed towards improving previous radar-radiometer comparisons by aligning the CaPE AMPR imagery with the radar-derived hydrometeor profiles and radiative transfer model results (Vivekanandan et al., 1990). The relative sensitivity of the various AMPR channels to the columnar integrated rain, mixed phase, and ice water contents and rain rates is presented. The CP-2 radar derived hydrometeor drop size distributions (DSD) are outlined in Section 4, and microwave radiative transfer model results using the radar-derived DSDs are presented in Section 5. Part II will focus upon application of a multispectral cloud model-based hybrid precipitation retrieval algorithm (Smith et al., 1992; Mugnai et al., 1993) to the same AMPR measurements investigated here. The two approaches will be compared for consistency.

## 2. AMPR and Radar Instrumentation During CaPE

The AMPR is specifically assembled to mount and operate within the lower pod of an ER-2 aircraft (Spencer et al., 1993). It utilizes the identical

multifrequency feedhorn (MFFH) as the current DMSP Special Sensor Microwave/Imager (SSM/I) for its 19.35, 37.1, and 85.5 GHz channels, with a separate feedhorn for the 10.7 GHz channel. For brevity, we will refer to these as the 10, 19, 37, and 85 GHz channels. A flat reflective plate is used to direct the upwelling scene emission through a dielectric lens/feedhorn assembly. Nadir resolutions on the Earth's surface are 2.8 km at 10.7 and 19.35 GHz (these two channels have matched beamwidths), 1.5 km at 37.1 GHz, and 640 meters at 85.5 GHz. A stepper motor spins the reflector such that the observed scene is scanned across-track, starting at $+45°$ from nadir (pilot's right), through nadir out to $-45°$ (pilot's left), and then repositions itself at $+45°$ and repeats. Each scan/reposition cycle requires 3 seconds, during which time the aircraft moves forward about 700 meters. After every fourth scan, the reflector moves up into a "stare" mode while alternately viewing hot and cold reference loads. The scan rate is sufficient to provide contiguous mapping at 85.5 GHz, with spatial oversampling occurring for the three lower frequencies. With an receiver integration time of 50 ms, enough time is available for fifty integrator samples across-track. For an ER-2 flight altitude of 20 km, the total across-track swath width on Earth is $\approx 40$ km.

Unlike the SSM/I, the AMPR currently uses a single MFFH port for each of the channels, with the feedhorn axes mounted such that the receive polarization state at nadir is linear 45°. Consequently, the receive polarization state is always linear, changing from fully horizontal ($H$) at the scan start to fully vertical ($V$) at the scan end (i.e., moving along the equator of the Poincare sphere). A rotating polarization basis of the instrument causes a skew of the instrument's polarization basis with respect to the scene's polarization basis (Gasiewski and Kunkee, 1992). With the current AMPR feedhorn configuration and a single receiver per frequency, it provides true scene $H$ and $V$ $T_B$ only at each of its scan endpoints. However, its polarization state always remains a linear combination of the scene $H$ and $V$ across the scan according to

$$T_B(\theta) = T_B^H \cos^2(\theta - 45°) + T_B^V \sin^2(\theta - 45°) \quad (1)$$

where $\theta$ ranges from 45° at the scan start to $-45°$ at the scan end, and $T_B^H$ and $T_B^V$ are the $H$ and $V$ $T_B$ in the scene polarization basis. Using 10.7 GHz AMPR scans over a cloud-free ocean, Vivekanandan et al. (1993) employed Eq. 1 with a radiative transfer model and demonstrated agreement to within $\pm 2$ K across the scan. The degree of polarization change remains minimal within $\pm 15°$ of nadir.

In time synchronization with the ER-2 overflights, measurements were gathered with the National Center for Atmospheric Research (NCAR) CP-2 dual-frequency, dual-polarization radar system. The CP-2 radar operates in a linear polarization basis at both $S$ (3 GHz) and $X$ (10 GHz) frequency bands (Bringi and Hendry, 1990). At $S$ band, a high-power ferrite circulator is used to alternate the receive and transmit polarization states between horizontal ($H$) and vertical ($V$) polarization states with a 1 ms PRT, enabling the measurement of the differential reflectivity $Z_{DR} = 10\log(Z_H/Z_V)$ where $H$ and $V$ refer to the associated copolar reflectivity factors in $\text{mm}^6\,\text{m}^{-3}$. The $X$ band data are not employed here, due to rapid propagation attenuation towards the receiver noise floor before ever reaching the storm core region. For a discussion of the $X$ band CP-2 measurements and their application to radiometric observations of hailstorms, we refer to the analysis performed by Fulton and Heymsfield (1991).

## 3. AMPR and Radar Imagery During CaPE

Early flight lines during 12 August 1991 from 2030–2200 UTC concentrated on a large precipitating complex located approximately 100 km south of the CP-2 radar. The bulk of the precipitation was over land just inland from the Atlantic coastline, but slowly moved to the east over the Atlantic Ocean after 2130 UTC. This lengthy range from the radar increases the maximum dimension of the radar resolution volume to $\approx 1.7$ km along azimuth and elevation directions. Although this is not an ideal situation, the relatively coarse scale is comparable or better than the nadir ground resolution of all AMPR channels except 85 GHz. Interpretation of the polarization measurements at this range is also hindered by antenna sidelobe effects. The net effect is a smoothing of the radar parameters as sucessive radar beams overlap each other, in much the same fashion that adjacent-pixel 10, 19, and 37 GHz AMPR channels oversample as the scan moves across-track.

The entire storm was scanned in a PPI mode within three minutes during each ER-2 overpass.

### 3.1 *Precipitation Over Land*

During 2059–2103 UTC, the ER-2 moved along a 25° flight bearing over a precipitating cloud structure centered ≈ 110 km south of the CP-2 radar, and headed over the Atlantic Ocean after 2104 UTC. The flight track covers an along-track distance of ≈ 50 km and is plotted in the 3 km $Z_H$ constant-altitude PPI (CAPPI) in Fig. 1. The coordinates are with respect to the CP-2 radar. The 10 km CAPPI (not shown) illustrates an unusually high reflectivity, widespread ice region. The first column in Fig. 2 displays the 4 channel AMPR color imagery during this four minute flight interval. The images are plotted with flight time along the abcissa and AMPR scanning angle along the ordinate, with the flight line along the nadir (0°) angle. At 10 GHz, the Atlantic ocean coastline is visible to the very lower right of the image through a series of tight contours between the radiometrically warm land (260–280 K) and the cool ocean (< 120 K).

Two main features are noted in against the warm land background. At 10 GHz, two 180 K regions are visible near the −30° angle, and near the center a region of 240 K is noted. The 19 GHz image shows that the features near the −30° scan angle have warmed with respect to 10 GHz, a trend associated with reduced emissivity wet soil (rain fallout from earlier storm passage) or the presence of surface water. The center region has cooled by 60 K with respect to 10 GHz, a trend usually associated with land-based precipitation. It is worth mentioning that the 19 GHz $T_B$ over the core (180 K) is comparable to the coolest 18 GHz $T_B$ observed during the COHMEX experiment (Adler et al., 1990), even though the viewing angles were different.

As frequency increases, the radiometer begins to respond to scattering processes located higher in the cloud, with the net result being an across-track "stretching" of the $T_B$ contours. For example, at the 20 km ER-2 altitude, the total across-track dimension for a constant feature at 10 km height is 20 km. This tendency is especially obvious in the 37 and 85 GHz images in Fig. 2. Near 2101, the 37 GHz 180 K $T_B$ contour extends over ±30

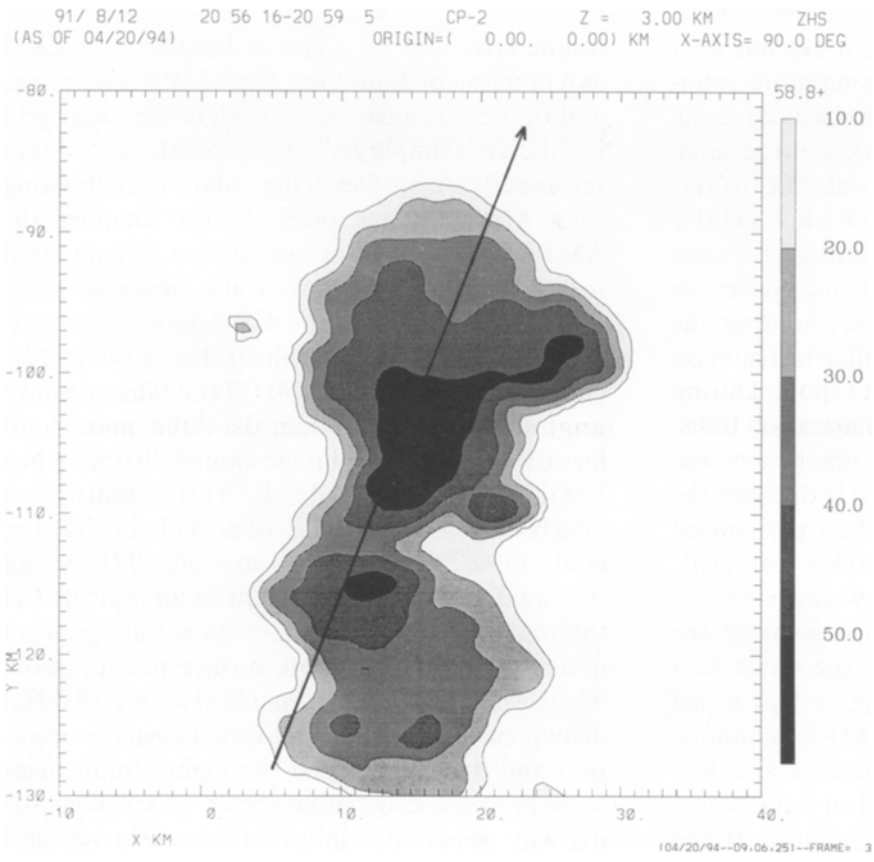


Fig. 1. Constant-altitude contours of the 3 GHz CP-2 radar reflectivity $Z_H$ in dBZ at a 3 km height, displaying the ER-2 aircraft track from 2059-2103 UTC

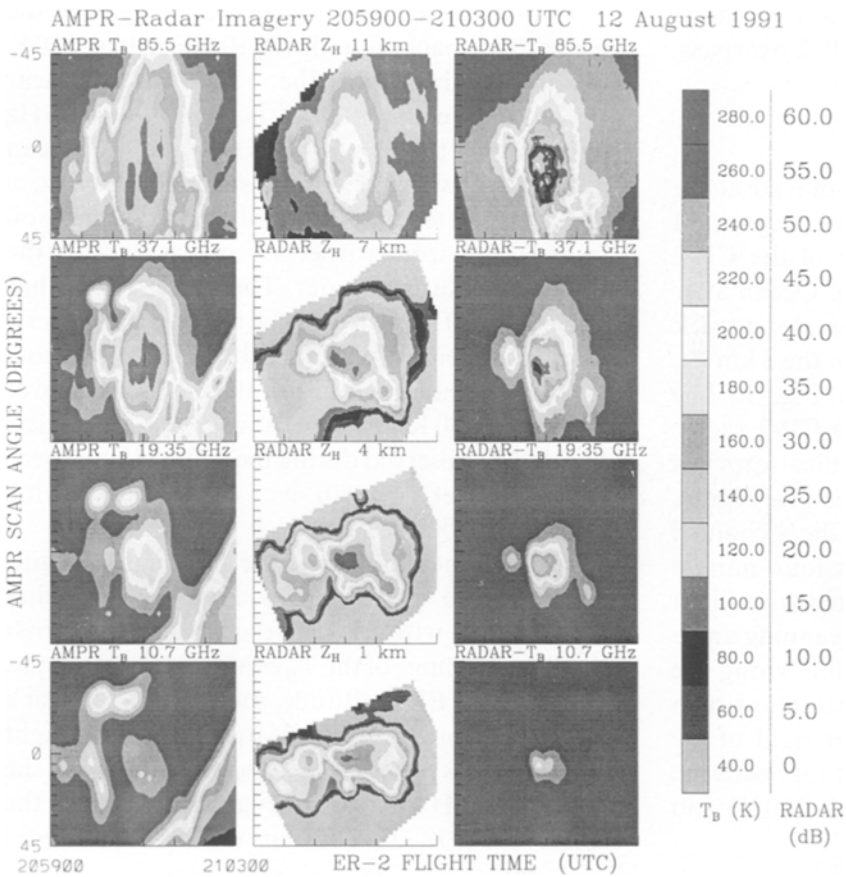


Fig. 2. Column 1: AMR imagery obtained on 12 August 1991 from 2059–2103 UTC along a 25° flight bearing 100 km south of the CP-2 radar. From bottom to top, the 10.7, 19.35, 37.1, and 85.5GHz channels are contoured in equivalent black-body brightness temperature ($T_B$) Kelvin units. AMPR imagery format displays the flight time along the abcissa, and the AMPR scan angle along the ordinate. Column 2: 3 GHz radar reflectivity imagery remapped to heights of 1, 4, 7, and 11 km above ground level into the same coordinates as Column 1. Column 3: Simulated AMPR $T_B$ obtained from using the radar-derived microphysics as input to a radiative transfer model (see Sections 4 and 5)

degrees of nadir, while at 85 GHz it extends over the entire scan. In addition to the main precipitation core in the image center, a smaller cell along nadir near 210030 UTC is evident, and the small bulge in the ocean-land boundary noted at 10 GHz is now fully enhanced in the 37 and 85 GHz images. At 85 GHz, any visible contrast between the land and ocean background disappears, as water vapor and cloud water surrounding the main cloud structure provide sufficient emission warming to produce a band of $T_B > 250$ K. During COHMEX, 92 GHz $T_B$ values of less than 100 K were often observed over storm cores, near the values noted here, while the 37 GHz $T_B$ over the core (120 K) is slightly warmer than the coolest 37 GHz COHMEX values of $\approx 100$ K (Adler et al., 1990), again with the different view angles.

In order to facilitate the comparisons of the AMPR and CP-2 measurements, the radar data were remapped into a coordinate system based upon the flight track and the AMPR scanning. The full radar PPI set of volume scans was interpolated into a cartesian grid of data points with the CP-2 radar feedhorn situated at the origin. Given the $(x, y, z)$ coordinates of the ER-2 as a function of flight time, the AMPR scan angle, and the $(x, y, z)$ locations of each of the radar grid points, it is a simple geometric operation to obtain the underlying profiles of the radar products along each AMPR image pixel. In this manner the AMPR and radar data can be directly compared in either the vertical, along-track, or across-track dimension. In Fig. 2, the CP-2 radar constant-altitude $Z_H$ contours are illustrated in the middle column at heights of 1, 4, 7, and 11 km above ground level. In particular, the three main cloud features in the 11 km image exceed 30 dBZ when 85 GHz $T_B$ falls below 160 K. This similarity has also been noted by others (Adler et al., 1991; Adler et al., 1990; Fulton and Heymsfield, 1991). Using the radar image at 1 km height as an indicator of the rain rate, only AMPR scans within $\pm 20°$ of nadir intercept significant surface precipitation. The lower frequency channels (10 and 19 GHz) display only marginal contrast between precipitation and the surface, and the higher frequencies sense processes originating above $\approx 5$ km, illustrating why passive precipitation retrieval over land

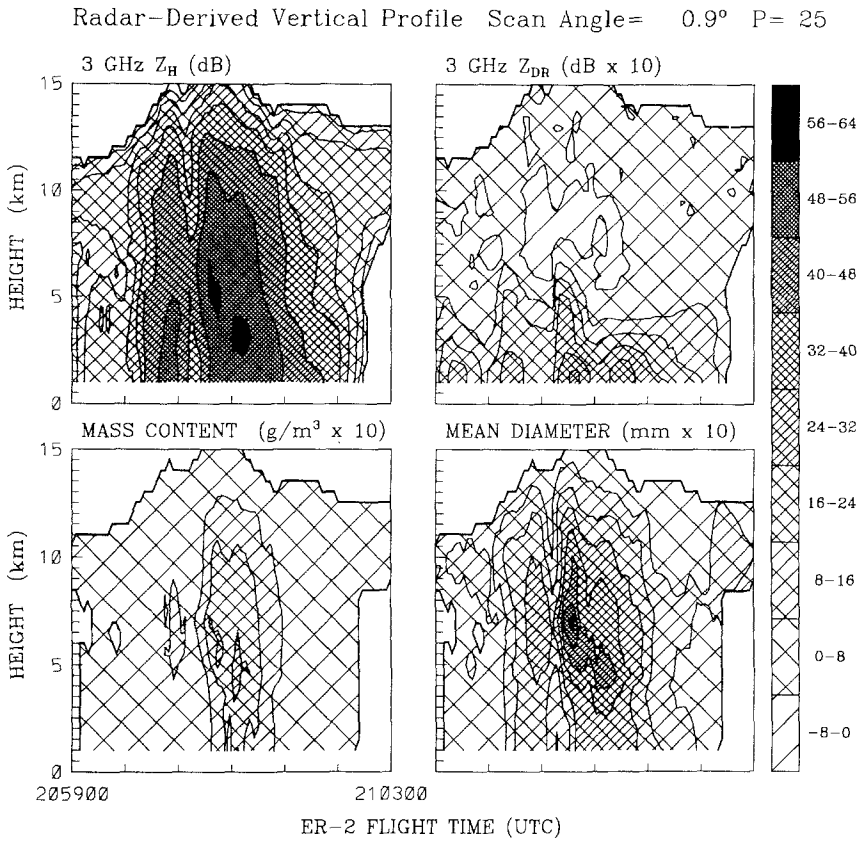


Fig. 3. Radar and radar-derived vertical profiles under the near-nadir AMPR trace. The flight time (2059–2103 UTC) is along the abcissa, and height is along the ordinate. Clockwise from upper left: 3 GHz $Z_H$ in dBZ, 3 GHz $Z_{DR}$ in dB × 10, radar-derived mean particle diameter in mm × 10, and radar-derived mass content in g m$^{-3}$ × 10

is more difficult than over ocean. Furthermore, with fine-scale radiometric resolution and an oblique viewing angle, it is possible to obtain 37 and 85 GHz $T_B$ depressions over a precipitation-free region. Directly over the main core, the 37 and 85 GHz $T_B$ fall to near the same value of $\approx$ 100 K, with 37 GHz $T_B$ < 85 GHz $T_B$ in some instances. This feature was also noted in other ER-2 flights (Vivekanandan et al., 1993).

The upper panels of Fig. 3 provide vertical profiles of the radar $Z_H$ and $Z_{DR}$ as a function of flight time under across-track pixel 25 (near-nadir). Radar data were not available below 1 km height. At 15 km above ground level, the cloud tops still exhibit near 25 dBZ echoes, and the deep, wide ice region covering this cloud is visible, including an anvil region past 210240 UTC. Extended, tall reflectivity columns are present at locations where the two main precipitation regions are located, 2100 and 2101 UTC. In both situations the 40–48 dBZ contour is present up to 12 km height, due to strong vertical air motion within the core. The profile of $Z_{DR}$ is consistent with this scenario. Positive $Z_{DR}$ extends up to 6–7 km height in the core regions, where large wet graupel or hail coexist with cloud water above the 0 °C isotherm level. Outside of the cores, where vertical air motion is reduced, the 0 dB $Z_{DR}$ contour remains at a height of near 4–5 km, where onset of melting occurs. $Z_{DR}$ gradually approaches 3–4 dB at 1 km height as the ice melts into oblate shaped rain drops with their major axes closely aligned along the horizontal. With this extended vertical structure, it is perhaps not suprising that internal scattering processes are intense enough to depress the 19 GHz $T_B$ below 180 K. A region of slightly negative $Z_{DR}$ is present directly over the main core between 6 and 11 km height, which has been associated with regions of hail (Bringi et al., 1986).

Aside from an obvious correlation between the radar and AMPR images, it is dificult to establish any quantitative relationships between either rainfall or ice content and the corresponding multi-frequency $T_B$. Although polarimetric observables such as $Z_{DR}$ possess significant dynamic range in rain, the 3 GHz radar polarimetric signatures associated with convective ice regions are usually quite weak.

### *3.2 Precipitation Over Ocean*

After 2100 UTC, the ER-2 continued repeat passes over several storm cells near the coastline 100 km

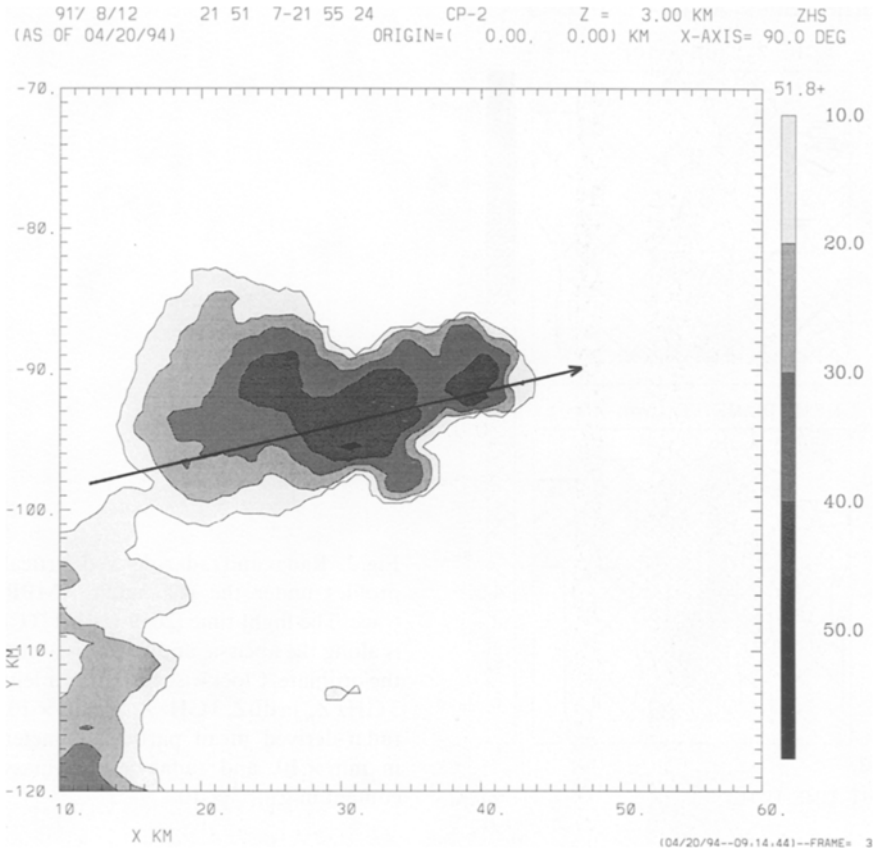


Fig. 4. Constant-altitude contours of the 3 GHz CP-2 radar reflectivity $Z_H$ in dBZ at a 3 km height, displaying the ER-2 aircraft track from 2152–2155 UTC

south of CP-2. By 2150, the storm depicted in Fig. 1 had broken apart, with the main core over the Atlantic Ocean, near the city of Melbourne. In Fig. 4, the 3 km CAPPI shows weaker reflectivities (peak value of 52 dBZ), and the remainder of the storm structure to the southwest over land with a much more widespread, but weaker reflectivity ice region than the land-based storm discussed above. The ER-2 flew along a 79° bearing directly over the core region of this storm. Figure 5 displays the AMPR color imagery in which the ER-2 crosses from land to ocean near 215315 UTC. The portion of the precipitation band over the ocean is of particular interest, as best seen in the 10 GHz AMPR image.

The rainfall over ocean exhibits a 10 GHz $T_B$ warming against the cool ocean surface, while the rainfall over land is not noticeable except for effects stemming from the 10 GHz spatial oversampling (aliasing) that occurs near the land-ocean coastline, where the contour lines are tightly packed together. This is an artifact of the changing fraction of land and ocean surface that is captured within the relatively large 10 and 19 GHz 2.8 km footprints while scanning near a land-ocean boundary. For the finer resolution 37 channel, the effect is slightly evident, although water vapor and cloud water absorption obscure the surface presence. Being an emission-based frequency, 10 GHz $T_B$ remains below 240 K for all rain rates encountered, while the 19 GHz $T_B$ saturates at near 260 K over a band along nadir. Since a calm ocean emissivity is lower at $H$ polarization ($+45°$ scan end), the $T_B$ gradually warms as the scan moves towards $V$ polarization ($-45°$ scan end). The polarization skew effect becomes less pronounced as the frequency increases due to atmospheric water vapor and surrounding cloud water partially masking the underlying ocean. The 37 GHz image is deceiving since a break in the 200–220 K contour (orange-red) occurs where the scattering-induced $T_B$ depression near 180 K is about equal to the $T_B$ from the non-raining part of the image (Smith et al., 1993). To the right of this feature, the less intense raining region near 2154 UTC has saturated the 37 GHz channel to near 260 K (reddish colors), where ice scattering effects are not yet dominant. In the middle column of Fig. 5, the

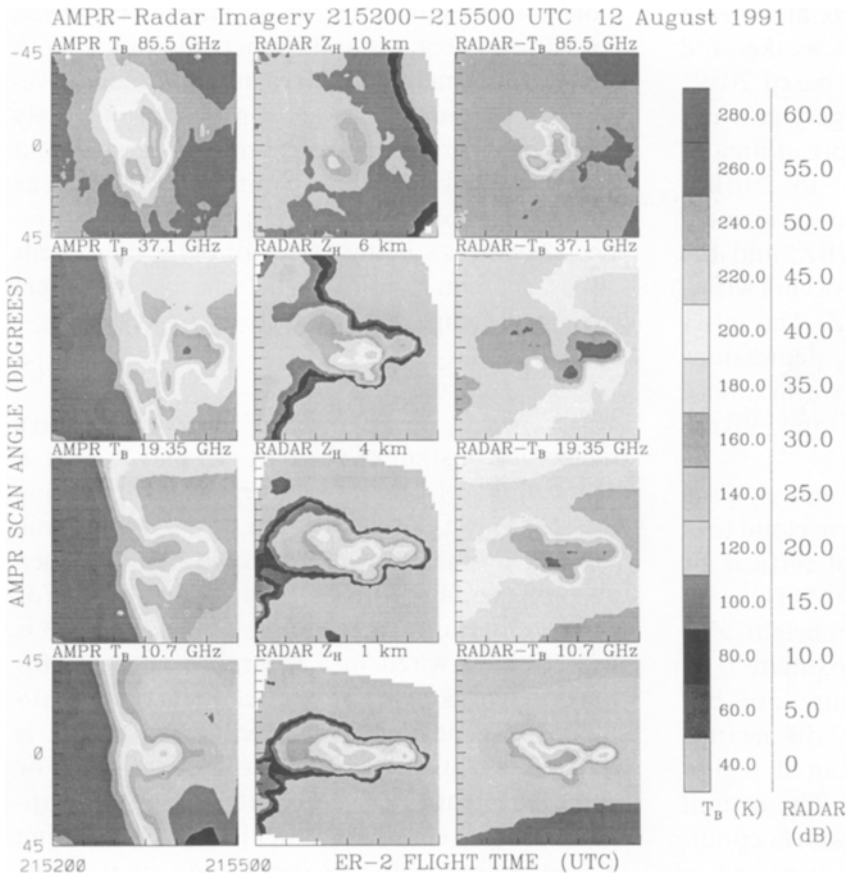


Fig. 5. Same format as Fig. 2, except the ER-2 flight time extends from 2152–2155 UTC along a 79° ER-2 flight bearing 100 km south of the CP-2 radar

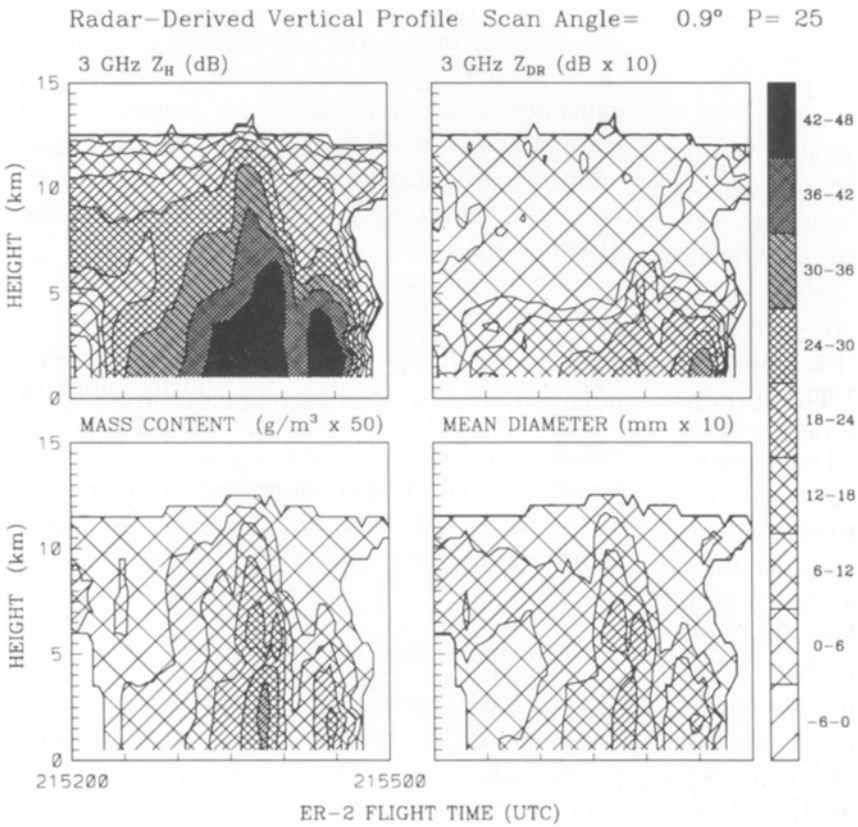


Fig. 6. Same format as Fig. 3, except the flight time extends from 2152–2155 UTC. Clockwise from upper left: 3 GHz $Z_H$ in dBZ, 3 GHz $Z_{DR}$ in dB × 10, radar-derived particle diameter in mm × 10, and radar-derived mass content in g m$^{-3}$ × 50

radar $Z_H$ images at heights of 1, 4, 6, and 10 km are shown. At this time, the storm is weaker and cloud tops are lower than the land-based 2059–2103 UTC time period. The $Z_H$ imagery at 6 and 10 km height depict the very widespread area of ice producing weak radar echoes of 15–20 dBZ. Two regions of 85 GHz $T_B < 160$ K are associated with identical regions of $Z_H > 30$ dBZ, and the surrounding region of $\approx 240$–$260$ K occurs with a widespread area of $Z_H \approx 15$–$20$ dBZ. The latter feature is perhaps due to slight $T_B$ depressions from small ice particles scattering the warm surface emission and water vapor (Evans and Vivekanandan, 1990).

The vertical profiles of radar $Z_H$ and $Z_{DR}$ are shown in the top panels of Fig. 6, where cloud tops remain steady at 12 km. Evidence of vertical air motion is present in $Z_H$ near 215330 UTC, with some 30 dBZ echoes present at 11 km height. $Z_{DR}$ is slightly positive above the approximate 0 °C level of 4–5 km only within the main core, but otherwise steadily increases to 2–3 dB nearest the surface. A portion of the ice anvil region is noticeable from 2152–2153 UTC. The overall measurements suggest a less intense storm condition than the land-based overflight discussed in Section 3.1.

## 4. Inversion of Radar Data into Hydrometeor Profiles

From the radar data, the desired physical retrievals include the columnar liquid, melting, and frozen mass contents, as well as the surface rain rate. Yet these quantities can be constituted by widely varying particle size distributions which yield vastly different microwave radiometric behavior.

In addition to the mass content $M$, radiative transfer applications require knowledge of the drop size distribution underlying the various particle types throughout the cloud. Unlike raindrops, the density, size, and shape of frozen ice particles vary widely with regard to cloud type and temperature, and published $Z - M$ ice relations vary widely. Also, it is not often clear whether the $Z - M$ relation refers to the radar reflectivity factor $Z$ (proportional to the sixth moment of the ice size distribution) or the equivalent radar reflectivity factor $Z_e$ (which is closer to what is actually measured and displayed). Since rain and ice hydrometeors are generally nonspherical, the radar polarization state must be stipulated. However, for snow aggregates and aspherical graupel with dimensions small compared to the radar wavelength, the radar cross section is approximately that of a sphere of equivalent mass (Marshall and Gunn, 1952). For radars operating in a dual linear ($H$ and $V$) polarization basis, the horizontal reflectivity $Z_H$ is a better indicator of the equivalent sphere $Z_e$ than $Z_V$. For particles whose diameters are small compared with the radar wavelength,

$$Z_e = (|K|/|K|^2_{\text{rain}})\, Z \tag{2}$$

where $K = (\varepsilon_r - 1)/(\varepsilon_r + 2)$, $\varepsilon_r$ being the relative dielectric constant of the particle, and $Z_e$ and $Z$ are in units of $\text{mm}^6\,\text{m}^{-3}$. For rain drops fitting this condition, $Z_e \approx Z$ (Smith, 1984). In general, the appropriate value of $\varepsilon_r$ should be used when encountering hydrometeors other than rain. For meteorological radars, a value of $|K|^2_{\text{rain}} = 0.93$ is usually hard-wired into the radar constant for purposes of converting the received power into the equivalent radar reflectivity. For ice, $\varepsilon_r$ is essentially a function of the particle density $\rho$. For a particle matrix of ice + water, $\varepsilon_r$ quickly approaches that of rain for water fractions exceeding 5%, regardless of the ice density. As an example, for $\rho = 0.6\,\text{g cm}^{-3}$, $Z_e$ is less than $Z$ by about 10 dB, but with 5% melt water added, this difference decreases to only 4 dB. The following computations assume that the radar targets consist of equivalent spherical particles with diameters small compared to the 10 cm radar wavelength, and adopt $Z_H$ as a measure of $Z_e$. Under such conditions the reflectivity is a function of the size distribution parameters alone. Earlier work involving one of the authors has accounted for the $H$ and $V$ polarized $T_B$ from ice crystals such as needles and plates (Evans and Vivekanandan, 1990). While we recognize the shortcomings of using an equivalent volume sphere approach to radiative transfer modeling of precipitation, it is a secondary effect when compared to the impact of the ice size distribution upon $T_B$, itself still being a largely unknown effect.

### *4.1 Inversion Algorithm Description*

The inversion method relies upon extrapolating the drop size distribution parameters from one point to the next while maintaining consistency with the observed CP-2 reflectivity. This allows

for smooth transitions to take place in the DSD and mass content when moving between rain and ice, eliminating the discontinuity encountered when applying different $Z-M$ relations for rain and ice. With this scheme it is necessary to stipulate the directions that the DSD parameters change with respect to a change in reflectivity. The result is a consistent, but non-unique hydrometeor structure. A gamma drop size distribution (DSD) truncated at $D_{\max} = 10\,\text{mm}$ is used,

$$N(D) = N_0 D^m \exp(-\Lambda D) \quad \text{mm}^{-1}\,\text{m}^{-3} \tag{3}$$

where $N_0$ is the intercept in units of $\text{mm}^{-(1+m)}\,\text{m}^{-3}$, $\Lambda$ is the slope in $\text{mm}^{-1}$, and $m$ is the shape factor, often referred to as the dispersion factor. As $m$ increases $>0$, the mode of the size distribution shifts to a larger size. In this case, the radar inversion process can be stated as:

$$[Z_H, Z_{DR}] \Rightarrow [N_0, m, \Lambda] \tag{4}$$

For ice, we assume a fairly high particle density of $\rho = 0.75\,\text{g cm}^{-3}$. In between the ice and rain regions, a region of wet ice is assumed to exist with an included water fraction $f_w$, where $0 \leqslant f_w \leqslant 1$.

After obtaining the radar profile underlying each pixel in the AMPR images as discussed in Section 3.1, the values of $Z_H$, $Z_{DR}$, and the height are used to assign each point along the profile as rain, ice, or a mixture composed of wet ice. A $Z_H >$ 10 dBZ threshold was applied. The ice region extends from the region where $Z_{DR}$ falls to near 0 dB up to the 10 dBZ cloud top, while the top of the rain region extends up to 3–4 km height. In some high $Z_H$ regions, the rain region may only extend up to 3 km height when a mixture of rain and ice (such as hail) reduces the $Z_{DR}$ below that typically expected for the associated $Z_H$ assuming pure rain (Chandrasekar et al., 1991). In between the all rain and all ice regions lies a band of variable, but positive $Z_{DR}$ that is assumed to be composed of an ice + water matrix. This category is referred to as the mixture or mixed phase region.

The procedure starts from the core region of the storm and spreads radially outward until all points are processed. To initialize each profile, the rain point nearest the surface is located and initial values of the shape parameter $m$ and intercept $N_0$ are assigned. The slope $\Lambda$ is then calculated such that the final DSD agrees with the radar-measured $Z_H$,

$$[N_0, m, \Lambda, \rho] \Rightarrow Z_H = Z_e, \tag{5}$$

where the arrow indicates that the DSD on the left is numerically consistent with the radar value on the right side. $Z_H$ is the observed CP-2 value in units of $\text{mm}^6\,\text{m}^{-3}$, which we have adopted as the measure of the equivalent sphere $Z_e$ calculated by,

$$Z_e = \frac{|K|^2}{(0.93)} \int_0^{D_{\max}} D^6 N(D) dD \quad \text{mm}^6\,\text{m}^{-1} \tag{6}$$

The associated mass content $M$, mean particle size $D_m$ and rain rate $R$ at a 1 km height are also calculated,

$$M = \frac{\pi\rho}{6000} \int_0^{D_{\max}} D^3 N(D) dD \quad \text{g m}^{-3} \tag{7}$$

$$D_m = \int_0^{D_{\max}} DN(D) dD \Big/ \int_0^{D_{\max}} N(D) dD \quad \text{mm} \tag{8}$$

$$R = (0.0036)\frac{\pi}{6} \int_0^{D_{\max}} D^3 v(D) N(D) dD \quad \text{mm hr}^{-1} \tag{9}$$

where $v(D)$ is the terminal fallspeed in $\text{m s}^{-1}$ (Doviak and Zrnic, 1984).

For $Z_H < 35\,\text{dBZ}$, $m = 0$ and $N_0 = 8000$ $\text{mm}^{-1}\,\text{m}^{-3}$. For $Z_H > 35\,\text{dBZ}$, $N_0$ was allowed to decrease with increasing $Z_H$ while $m$ is allowed to vary between 0 and 5 for rain, increasing as $Z_H$ increases. While the latter is a bold assumption, it is consistent with the range of $m$ values found by several investigators (Ulbrich, 1983; Russchenberg and Ligthart, 1991). Overall, these assumptions assume that as $Z_H$ increases, the associated DSD moves from an exponential, fixed $N_0$ condition into a narrower gamma distribution with the mean particle size shifted upwards. If there are no rain points along the profile (such as when viewing through the anvil portion of the cloud), the nearest adjacent point is located and the DSD is extrapolated from this as described below. For points flagged as wet ice, the water fraction $f_w$ is computed so as to complete a smooth transition in $Z_e$ between the rain and ice regions, thereby avoiding any gross discontinuities in the vertical mass content and the DSD parameters.

The algorithm then works upward, extrapolating the desired DSD parameters $N_0$, $m$, and $\Lambda$, from the nearest already-assigned point (usually the one below it). This allows for smooth transitions to take place in the DSD when moving from one hydrometeor category to another without

having to apply a $Z - M$ relation for ice. Denoting the known and unknown points with the subscripts 1 and 2, respectively, then the known point is defined by

$$[N_{0,1}, m_1, \Lambda_1, \rho_1] \Rightarrow Z_{H,1} = Z_{e,1}. \quad (10)$$

The known DSD parameters are then perturbed in incremental amounts $\Delta$ about their assigned values in such a fashion that

$$[N_{0,1} \pm \Delta N_0, m_1 \pm \Delta m, \Lambda_1 \pm \Delta\Lambda, \rho_2] \Rightarrow Z_{H,2} = Z_{e,2}, \quad (11)$$

where $\rho_2$ and $Z_{H,2}$ are the density and $Z_H$ associated with the unknown point 2. The assumption made here as that $\Delta m > 0$ if $Z_{H,2} > Z_{H,1}$, and $\Delta\Lambda < 0$ if $Z_{H,2} > Z_{H,1}$. In other words, $m$ and $\Lambda$ increase and decrease, respectively, with increasing $Z_H$. From this locally-derived set of potential DSD candidates, local $Z_e - m$ and $Z_e - \Lambda$ relations are found, from which the final $m_2$ and $\Lambda_2$ are calculated using the value of $Z_{H,2}$. Lastly, the intercept $N_{0,2}$ is calculated so as to produce agreement with the the radar-measured $Z_{H,2}$

$$[N_{0,2}, m_2, \Lambda_2, \rho_2] \Rightarrow Z_{H,2} = Z_{e,2}. \quad (12)$$

The associated mass content $M_2$ is calculated using Eq. 7 with the value of $\rho = \rho_2$.

The procedure then continues to process all profiles underneath all AMPR pixels, spreading out from the starting location until finished. Since the reflectivities generally decrease away from the core region, the shape factor $m$ gradually is reduced to zero near the cloud top and edges, and the DSD approaches the exponential ($m = 0$) case. While this procedure obviously does not produce a unique gamma DSD, it is however numerically consistent with the measured $Z_H$ throughout the entire grid, assuming that the particles are modeled as equivalent spherical shapes.

### 4.2 *Radar-Derived Hydrometeor Structure Over Land*

In the bottom two plates of Figs. 3 and 6, the vertical profiles of the mass content and mean particle diameter are displayed for the nadir traces of the land and ocean-based storms, respectively. In general, the profiles are in qualitative agreement with what one would expect for the vertical profiles of the $Z_H$ and $Z_{DR}$ radar products shown above them. The land-based case produces peak

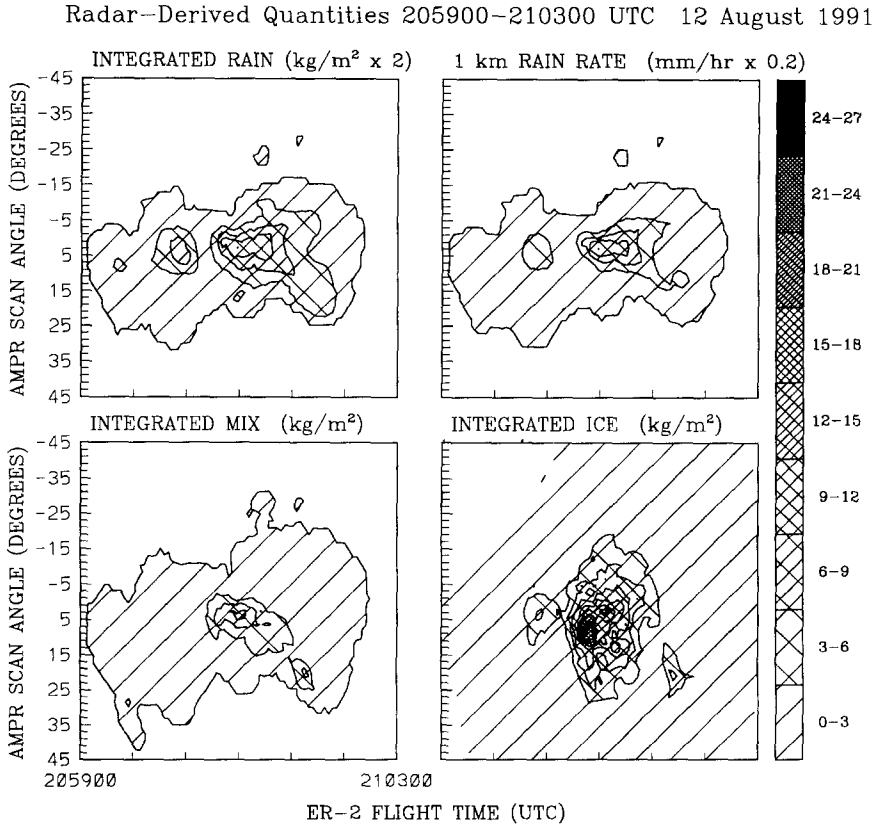


Fig. 7. Radar-derived columnar integrated water paths for the 2059–2103 UTC flight segment. The flight time is along the abscissa and the AMPR scan angle along the ordinate. Clockwise from upper left- integrated rain water path (RWP) in kg m$^{-2}$ × 2, rain rate at 1 km height in mm hr$^{-1}$ × 0.2, integrated ice water path (IWP) in kg m$^{-2}$, and integrated mixture water path in kg m$^{-2}$

mass contents of 2–3 g m$^{-3}$ from 3–6 km height, slightly above where the peak $Z_H$ occurs, although the mass content is perhaps slightly too large near 11–13 km above the core. The associated mean particle size $D_m$ computed from the DSD ranges from 4–5 mm diameter in these same regions, with smaller values aloft and at the surface. This sizing is consistent with small wet hail and graupel near and above the freezing level, and eventual drop breakup into rainfall at heights below 3 km (Fulton and Heymsfield, 1991). The model results of Adler et al. (1991) produced rain and ice water contents up to 5 g m$^{-3}$ near the freezing level.

Figure 7 depicts the columnar integrated rain, mixture, and ice contents in units of kg m$^{-2}$ for the entire storm in the same type of format as the color images in Fig. 2 (flight time along abcissa, AMPR scan angle along ordinate). Near 2100 and 2101 UTC, the integrated rain water path (RWP) peaks at 7 kg m$^{-2}$ very close to the nadir trace, near the $-5°$ scan angle. The integrated mixture and ice water paths (MWP and IWP) peak at 7 and 25 kg m$^{-2}$, where the latter is suspected as an overestimate of the total IWP. In general, it is fair to state that radar retrieval of ice microphysics is still somewhat primitive due to poor parameterizations of the ice DSD and density. Nonetheless, the 85 GHz AMPR image displays a close correlation with the IWP image, with all three main ice regions associated with an 85 GHz $T_B$ depression as expected. Rainfall rates as derived by Eq. 9 are contoured in the upper right of Fig. 7, with peak rates of 60 and 20 mm hr$^{-1}$ found at the 1 km height within the main and secondary cores, respectively. In Part II of this article the radar-retrieved microphysics for the scans near nadir are compared with the output of a multispectral, vertical profiling precipitation retrieval algorithm with its own internal microphysics.

### *4.3 Radar-Derived Hydrometeor Structure Over Ocean*

For the ocean-based storm, the mass content values are smaller, as one might suspect from the vertical profiles of the $Z_H$ and $Z_{DR}$, and the 85 GHz AMPR image (Fig. 6). Peak mass contents here are on the order of 0.8 g m$^{-3}$ in and above the rain column, where $Z_{DR}$ pops up above the 4–5 km freezing level (note the scaling factor for

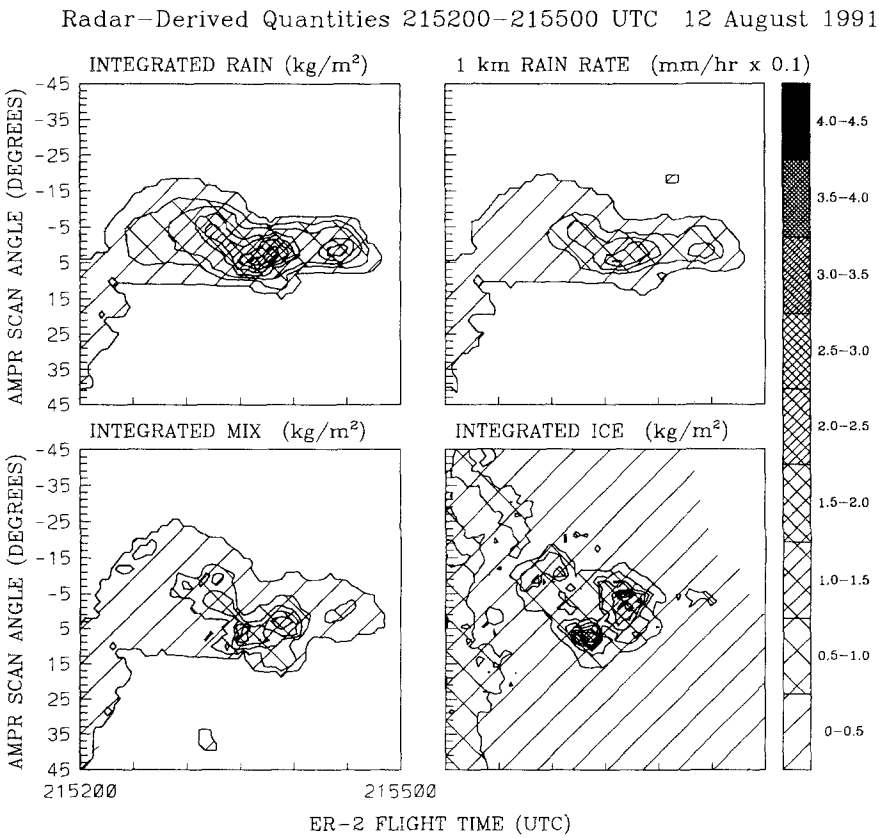


Fig. 8. Same format as Fig. 7, except the flight time extends from 2152–2155 UTC. Clockwise from upper left: integrated rain water path (RWP) in kg m$^{-2}$, rain rate at 1 km height in mm hr$^{-1}$ x 0.1, integrated ice path (IWP) in kg m$^{-2}$, and integrated mixture water path in kg m$^{-2}$

the contours). The mean particle diameters are $\approx 1.5$ to 2.5 mm in the core, while in the ice anvil region from 2152–2153 UTC, the mean particle diameter is within the 0.6 to 1.2 mm contour bin.

Associated columnar rain, mixture, and ice water paths are presented in Fig. 8. All three categories are below 3.5 kg m$^{-2}$ columnar path, with once again the 85 GHz AMPR image displaying close correlation with the IWP. Both the two main regions of high IWP as well as the surrounding, widespread ice anvil region are manifested by scattering depressions in the 85 GHz AMPR image. There are two peaks in the rainfall rate of 20 and 13 mm hr$^{-1}$, while the IWP peaks to 2.5 kg m$^{-2}$ only for the main core, consistent with the storm structure noted in the radar $Z_H$ and $Z_{DR}$ vertical profiles.

### *4.4 Sources of Uncertainty and Error*

A comparison of the radar-retrieved IWP and the 37 and 85 GHz $T_B$ as measured by the AMPR (Figs. 2 and 7, respectively) shows that the near-nadir trace (across-track pixel 25) falls very near the edge of the storm core as best determined by radar. For nearby AMPR scans, the minimum 37 and 85 GHz $T_B$ changes very little for regions surrounding the storm core, maintaining itself near 100–120 K, while at the same time the radar-retrieved IWP changes by a factor of two.

Evidentally, the wide variability in the radar-derived microphysics is not manifested by the AMPR $T_B$. While some of this is undoubtedly due to the nonlinear relation between IWP and $T_B$, it is likely that some of this difference originates in several sources of uncertainty in the radar modeling. First, near nadir, across-track pixels 24 and 27 are displaced by only 3 km on the Earth's surface. Depending upon the cumulative number of turns that the ER-2 executes, its navigation can be off by up to 10 km during the latter stages of the flight. Second, since each AMPR channel responds to different regions in the vertical atmosphere structure, it was necessary to apply an offset to the AMPR navigation latitude and longitude, align its minimum $T_B$ regions with the region of peak radar $Z_H$ at each AMPR frequency, and determine a "best match" applicable to all four frequencies. Typical offsets were on the order of $\pm 0.01$ to 0.03 degrees (1–3 km on the Earth's surface) for the 12 August 1991 flights analyzed here. Third, with the lengthy range of these storm cells from CP-2 (110 km), the radar resolution along azimuth and elevation directions is as large as 1.7 km. This alone is nearly three times the nadir Earth resolution of the 85 GHz AMPR channel. Finally, one must take into account the spatial averaging that takes place when processing the radar volume scans into a Cartesian coordinate system at this range from the radar. In accounting for the location uncertainty only the nadirviewing results presented in Part II of this manuscript will be compared to the radar-derived values over several nearby AMPR traces.

## 5. Radar-Based $T_B$ Modeling

In addition to comparing the AMPR imagery against the radar-retrieved vertical cloud profiles, the radar-derived drop size distributions were used as input to a microwave radiative transfer model to simulate the AMPR imagery. A plane parallel microwave radiative transfer model employing Mie scattering phase matrices for spherical particles has been specifically adapted for use with radar-derived size distributions as its input (Vivekanandan et al., 1991). The model considers the full Stokes vector $[I, Q, U, V]$, allows for a polarized surface, and many layers of size distributions of particles types, including mixtures of types. Absorption by gaseous oxygen, water vapor, and cloud water is accounted for. Since the modeled atmospheric particles are spherically shaped, the Mie phase matrices contain only four independent elements. Consequently, any presence of the $Q$ component results from a polarized surface, such as a specular ocean surface, but can be related to the vertical ($V$) and horizontal ($H$) $T_B$ in the scene basis by $T_B^V = T_B^I + T_B^Q$ and $T_B^H = T_B^I - T_B^Q$. From these, the simulated AMPR $T_B$ can be found as a function of scan angle using Eq. 1. Quadrature integration over 16 streams per hemisphere and the method of doubling and adding (Evans, 1991) are used to solve the equation of transfer in a layered, scattering atmosphere. Surface temperature was set to 300 K, with the model accounting for surface reflection and emission from either a Lambertian land surface or a specular, polarized ocean. A typical moist adiabatic temperature lapse rate of 6 °C km$^{-1}$ was used with a surface air temperature of 30 °C. The layer spacing was set to 0.5 km up to 15 km height for a total of 30 layers.

Along the profile of points corresponding to each AMPR pixel, absorption and scattering cross sections were calculated using Mie theory, and integrated over the radar-derived size distributions to obtain the volume extinction coefficient and albedo. For the rain, mixture, and ice regions, the Legendre expansion coefficients describing the angular form of the four independent phase matrix elements are first found as a function of the scattering angle $\Theta$. The phase matrix elements are then transformed into a $(\theta, \phi)$, representation using the decomposition outlined by Kattawar et al. (1973), which simplifies the phase function integration by decoupling the $\phi$ dependence.

Cloud water plays an important role in modulating the TOA $T_B$ at all microwave frequencies for land and ocean-based storms (Smith et al., 1992; Adler et al., 1990). Radar backscattering is overwhelmed by precipitation-sized particles and therefore for modeling purposes, cloud water must be accounted for separately. A vertical profile of cloud water content $M_c$ was superimposed upon the radar-retrieved hydrometeor profile, defined as a function of temperature $T$ by

$$M_c(T) = M_0 e^{-a(T-T_0)^2} \tag{13}$$

where $M_0$ is the maximum amount of cloud water located at temperature $T_0$. The cloud water was added where the associated CP-2 radar $Z_H$ exceeded 5 dBZ. The factor $a$ is adjusted to vary the shape of the profile at temperatures above and below $T_0$. Cloud base was set at 1.5 km with an upper cloud cutoff at $T < -40\,^{\circ}\mathrm{C}$, and the surface relative humidity set to 80% and decreases linearly with temperature. For cloud liquid water drops small compared with the wavelength, the absorption coefficient is independent of the cloud drop size distribution, inversely proportional to the wavelength, and directly proportional to the mass content (Vivekanandan et al., 1991). The absorption increases quickly for $\lambda < 1$ cm, and also increases with decreasing water temperature. For example, at 85 GHz 1 g m$^{-3}$ cloud LWC at $-10\,^{\circ}\mathrm{C}$ yields a 1 km$^{-1}$ absorption coefficient. The water vapor and oxygen absorption are computed using the formulation presented by Liebe ( 1985).

### 5.1 *Radar-Derived $T_B$ Over Land*

For the 2059-2103 UTC land-based ER-2 overflight, the radar-derived $T_B$ images at the four AMPR frequencies are presented in color in column three of Fig. 2. To be consistent, a constant land emissivity $e = 0.9$ was assumed, rather than trying to model the highly variable surface emissivity for this ER-2 flight interval. The cloud liquid water profile used is defined by Eq. 13, where $M_0 = 0.5$ g m$^{-3}$ and $T_0 = -10\,^{\circ}\mathrm{C}$.

At 10 GHz, only the most intense part of the core region produces any noticeable scattering-induced $T_B$ depressions over the 260–280 K surrounding background, reaching a minimum of 210 K. The 19 GHz $T_B$ falls as low as 130 K over the core region, with the three main cloud features all displaying a $T_B$ depression. At 37 GHz, the 240 K contour is stretched across the scan near nadir, much like the AMPR 37 GHz image, with $T_B$ minima near 110 K. This results from the way the storm is modeled across-track. As the AMPR scan limits are approached, the radiative transfer computations are performed along a slant path that traverses the upper ice region, but misses the rain and mixture region directly below much of the ice. Since the 37 and 85 GHz radiative effects originate at higher regions of the cloud, the 37 and 85 GHz $T_B$ increasingly show depressions further away from nadir. Over land, the radar-derived imagery is consistent with the respective AMPR image in Fig. 2. Between 10 and 37 GHz, the AMPR $T_B$ varies between 240–280 K for the region surrounding the radar 5 dBZ echo level, a feature which is not manifested in the radar-modeled $T_B$. One might suspect the presence of widely variable surrounding cloud water. As expected, the model and AMPR image display the greatest discrepancies further away from nadir, where the limitations of plane-parallel atmospheric radiative transfer modeling are rapidly approached. However, for AMPR scans within $\pm 10$ degrees of nadir, the plane-parallel assumption appears sufficient and accurate for modeling purposes.

The nadir trace radar-derived $T_B$ is plotted in Fig. 9, where the monotonic decrease in the model $T_B$ with increasing frequency is evident for all points along track. Similar effects have been reported elsewhere (Adler et al., 1990). Also plotted at the bottom of Fig. 9 is the difference between the radar-derived and the AMPR $T_B$, with points after pixel 65 not comparable, as the ER-2 headed over ocean after this time. Positive and negative values indicate an overestimate and underestimate of the AMPR $T_B$, respectively. In general, all four

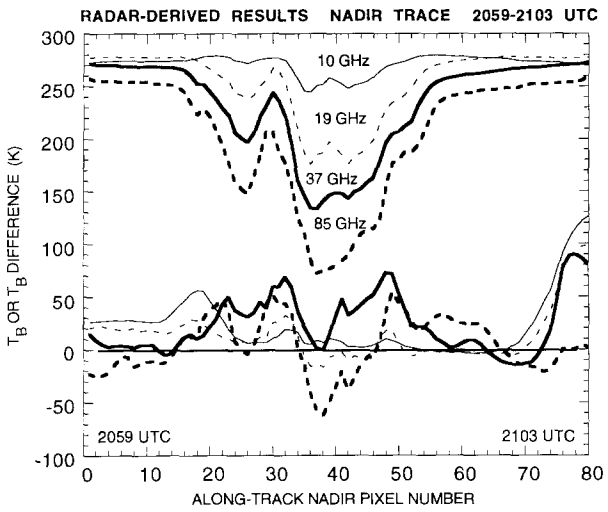


Fig. 9. Comparison of AMPR measured $T_B$ and the radar-derived $T_B$ along the near-nadir trace from 2059–2103 UTC, a total of 80 along-track pixels. Pixel 65 is the approximate boundary between land and ocean backgrounds. The top four curves illustrate the radar-derived $T_B$, and the bottom four curves centered about zero represent the difference between the radar-derived and measured $T_B$ in Kelvin units

radar-derived $T_B$ values overestimated the AMPR $T_B$ by as much as 70 K, with the one noteworthy exception being the interval between pixels 35 and 45. Here the 37 GHz radar-derived $T_B$ tended towards agreement with the AMPR $T_B$, while the 85 GHz $T_B$ underestimated the AMPR $T_B$ by up to 60 K.

The integrated ice water path (IWP) behavior is shown in the top panel of Fig. 10, where wide scatter is present in the radar-derived 85 GHz $T_B$ vs. total IWP (points plotted with a plus sign). Most of the scatter is due to the fact that a portion of the cloud water mixed throughout the ice, 85 GHz $T_B$ varies with the net radiometric effect of the cloud water mixed throughout the ice. saturating near 50 K beyond 20 kg m$^{-2}$. This plot is in quantitative accord witll results obtained independently by Adler et al. (1991), who used cloud model microphysics in their radiative transfer models. At this point, it is instructive to separate the region of ice that lies above the cloud water profile. The points plotted as circles in the top panel of Fig. 10 indicate this IWP amount, and the 85 GHz $T_B$ shows a tight relationship for IWP $< 4$ kg m$^{-2}$, after which the 85 GHz $T_B$ saturates near 50 K. The middle and bottom panels of Fig. 10 depict the 37–85 GHz $T_B$ difference as a function of the total IWP and IWP lying above

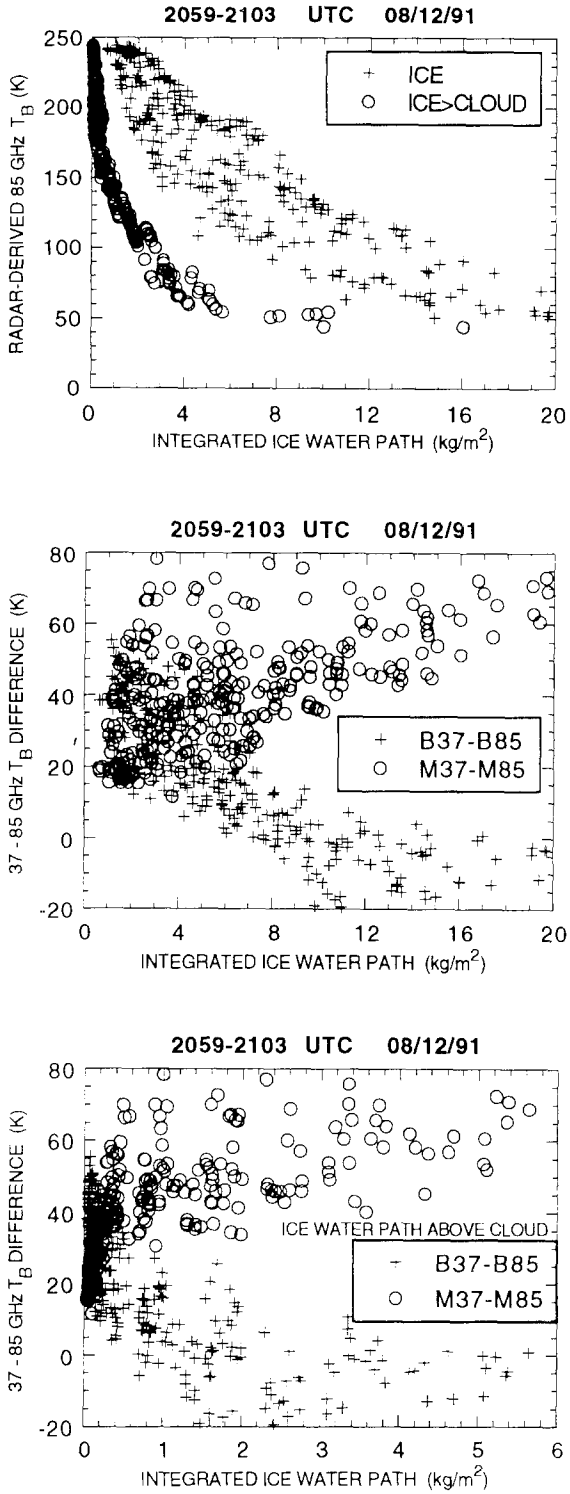


Fig. 10. Behavior of the columnar integrated ice water path (IWP) for the 2059–2013 UTC land-based storm. Only the points within $\pm 10$ degrees of nadir arc shown. Top: Radar-derived 85 GHz $T_B$ vs. total IWP (plus signs), and only the IWP lying above the cloud water (circles). Middle: 37–85 GHz $T_B$ difference vs. total IWP for the radar-derived 37–85 GHz $T_B$ (circles) and the AMPR measured 37–85 GHz $T_B$ (plus signs). Bottom: Same as the middle figure, except the IWP lying above the cloud water is considered

the cloud water, respectively. The AMPR measured and the radar-derived points are plotted with plus signs and circles, respectively. For the middle figure, nothing is obvious until the total IWP exceeds $6\,kg\,m^{-2}$, when the AMPR and radar-derived points continue in opposite directions. The AMPR 37–85 GHz $T_B$ difference moves below 0 K while the radar-derived points continue a positive trend. In the bottom figure, similar behavior is observed beyond $IWP > 0.5\,kg\,m^{-2}$. A good deal of wide scatter is evident in both of these figures, suggesting that the 37 GHz channel may be responding to regions below the ice where a mixed phase is present.

With such an extended vertical cloud structure, it is useful to know which particular AMPR channel is most sensitive to the presence of a mixed phase within precipitation, since the mixed phase region is usually a good indicator of the overall storm structure. In Fig. 11, the radar-derived 37 GHz $T_B$ is plotted as a function of the integrated mixture water path (MWP). Although wide scatter exists, a definite trend is present with sufficient dynamic range, suggesting that over land, the 37 GHz channel responds to heights where mixed phase precipitation is present. The 19 GHz channel suffers from a sufficient lack of contrast against the land surface, while the 37 GHz channel responds to processes deep enough within the cloud (especially over the core) and also provides enough $T_B$ dynamic range against the warm land. The response to the variable MWP provides an understanding of the lack of correlation with the total IWP in the 37–85 GHz $T_B$ differences (Fig. 10,

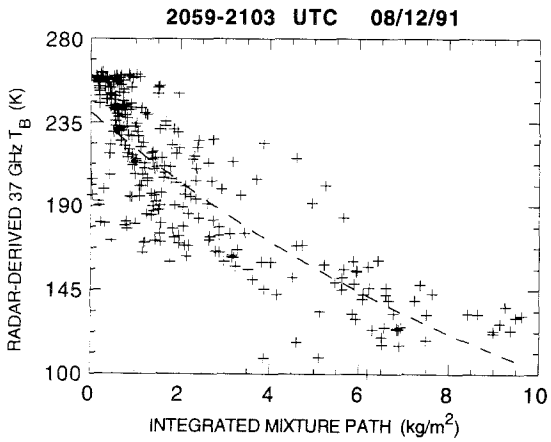


Fig. 11. Scatter plot of the radar-derived 37 GHz $T_B$ vs. the columnar integrated mixture path (IMP) for the 2059–2103 UTC flight time interval

middle and bottom). The radiative transfer model illustrates the inherent problem of retrieving mid-level columnar mass contents over a land surface. First the $T_B$ contributions from the emitting land surface must be overcome by enough mixed phase integrated mass content for scattering-based $T_B$ depressions to become dominant. Over the precipitating part of the cloud, the net upwelling $T_B$ profile remained near 280–290 K up to 4–5 km height regardless of frequency. However, as the region of mixed phase increases, the overlying frozen ice columnar content usually increases as well, and the net $T_B$ responds to ice scattering processes above the mixed phase region. In effect, the mixed phase region is quickly "bypassed" at AMPR frequencies as storm intensity increases.

### 5.2 *Radar-Derived $T_B$ Over Ocean*

For the 2152–2155 UTC ocean-based flight, the radar-derived $T_B$ images at the four AMPR frequencies are presented in color in column three of Fig. 5. In this modeling, the surface was modeled as a specular water layer, so that away from nadir, $T_B^V > T_B^H$, where the superscripts refer to the scene polarization state. Since the AMPR receive state moves towards the $V$ state across its scan, the modeled $T_B$ increases as a result, using Eq. 1. Therefore, comparisons with the AMPR imagery are applicable only after 2153 UTC, where the ER-2 moved out over ocean. The cloud liquid water profile used is defined by Eq. 13, where $M_0 = 0.3\,g\,m^{-3}$ and $T_0 = -5\,°C$. In general, the radar-derived $T_B$ are in much better agreement with the AMPR $T_B$ than noted for the previous land-based situation. At 10 GHz, the radar-derived $T_B$ shows a small region of 200–220 K near 215430 UTC, with the AMPR showing only a small region of 140–160 K (green), indicating lighter precipitation than the radar observed. However the 19 GHz image comparisons are in much closer agreement, with the radar-derived $T_B$ near 240–260 K over a larger extent than the AMPR $T_B$ shows. For both the 10 and 19 GHz radar-derived images, the scan-changing polarization state is nicely enhanced, and over the rain-free regions the associated $T_B$ shows quite good numerical consistency with the AMPR $T_B$.

At 37 GHz, there is a break in the 240–260 K contour nearly at the radar-derived $T_B$ image center, where the surface rainfall is near its peak

as shown in Fig. 8. A similar feature is noted in the actual 37 GHz AMPR image as well. This results when the scattering-induced $T_B$ depression over the intense storm core is of the same magnitude as the surrounding rain-free $T_B$. The small spot of 260–280 K near 2154 UTC and 15° scan angle is also noted in the 37 GHz AMPR image. Despite the shortcomings of the radar-derived ice microphysics, the 85 GHz images show a nice degree of agreement both in structure and relative $T_B$. The two regions of 85 GHz $T_B$ near 140–160 K are nearly co-located in both images, although once again the limitations of the plane parallel model are obvious away from $\pm 10°$ of nadir. Even though the radar-derived $T_B$ assumed an ocean surface everywhere, the surface characteristics are almost totally masked at 85 GHz. Unfortunately, neither the radar-derived nor the AMPR 85 GHz $T_B$ show much evidence of detecting the widespread ice anvil region where $Z_H \approx 20$ dBZ.

The nadir-trace radar-derived $T_B$ is plotted in Fig. 12, comparable to the AMPR $T_B$ after along-track pixel 25 when the ER-2 was always over ocean. The 37 GHz $T_B$ remains nearly saturated at 260 K with the exception of a $T_B$ depression over the main storm core. Even at 19 GHz, the $T_B$ saturates near 260 K and displays minimal contrast with the variable rain amounts shown in Fig. 8. The dynamic range of the 10 GHz channel clearly demonstrates the advantage of a channel which is relatively unaffected by scattering effects for measuring rainfall over ocean at these instrument resolutions. This observation is in close accord with results found independently by Smith et al. (1993). The TRMM instrument will include a 10.7 GHz channel.

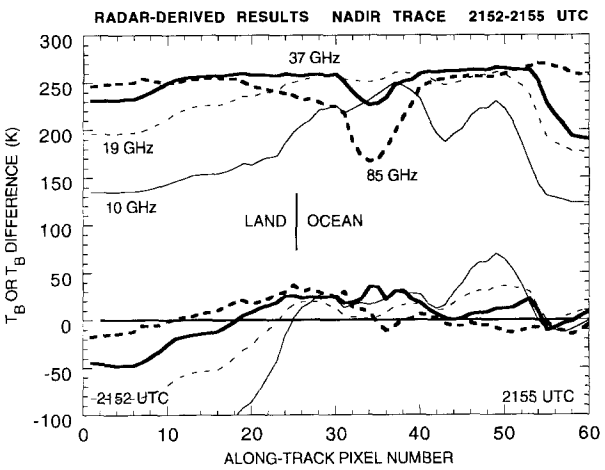


Fig. 12. Same as Fig. 9, except the flight time interval is from 2152–2155 UTC, a total of 60 along-track pixels. Pixel 25 is the approximate boundary between land and ocean backgrounds

The difference between the radar-modeled and the AMPR $T_B$ are also plotted in the bottom of Fig. 12, comparable after along-track pixel 25. As mentioned, the radar-derived 10 GHz $T_B$ overestimates the observed value by 60 K near pixel 48, which we have not been able to explain, though there appears to be a constant 25 K overestimate at 10 GHz across all pixels. The agreement amongst the remainder of the channels is quite satisfactory, overestimating the AMPR $T_B$ by no more than 25 or 30 K. In general, one would expect better agreement for the ocean-based precipitation, since emission and absorption processes are the dominant contributors to the radiative behavior below 37 GHz. These processes are less sensitive to variations in the drop size distribution than the scattering process (Jameson, 1991). Furthermore, much ocean-based precipitation exhibits weaker vertical velocities, with much less columnar ice water path, and extrapolating an ice size distribution from the underlying rain region is perhaps better founded under these circumstances. Since all of the $T_B$ differences here are within 30 K, it suggests that even with the assumptions and shortcomings of the radar inversion scheme, the radar-derived size distributions are good enough to be consistent with the observed radar and radiative behavior.

The added utility afforded by the 10 GHz channel is illustrated in Fig. 13, where the modeled 19 GHz $T_B$ is plotted as a function of the modeled 10 GHz $T_B$. Below 180 K, the points show a strong correlation, with additional scatter superimposed upon the relationship after 10 GHz $T_B > 180$ K. The points below this represent lighter rain rates, where the particle sizes lie in the Rayleigh regime at both frequencies and the absorption coefficient is inversely proportional to the wavelength. Above 10 GHz $T_B > 180$ K, ice particles increasingly exhibit Mie scattering effects at 19 GHz, which tends to depress the net upwelling $T_B$, in addition to the effects from cloud water, which tend to warm the net $T_B$. As a result the 19 GHz vs. 10 GHz $T_B$ trend displays scatter along either side of the mean trend.

A plot of the 10 and 19 GHz radar-derived $T_B$ as a function of the radar-derived rainfall rate is

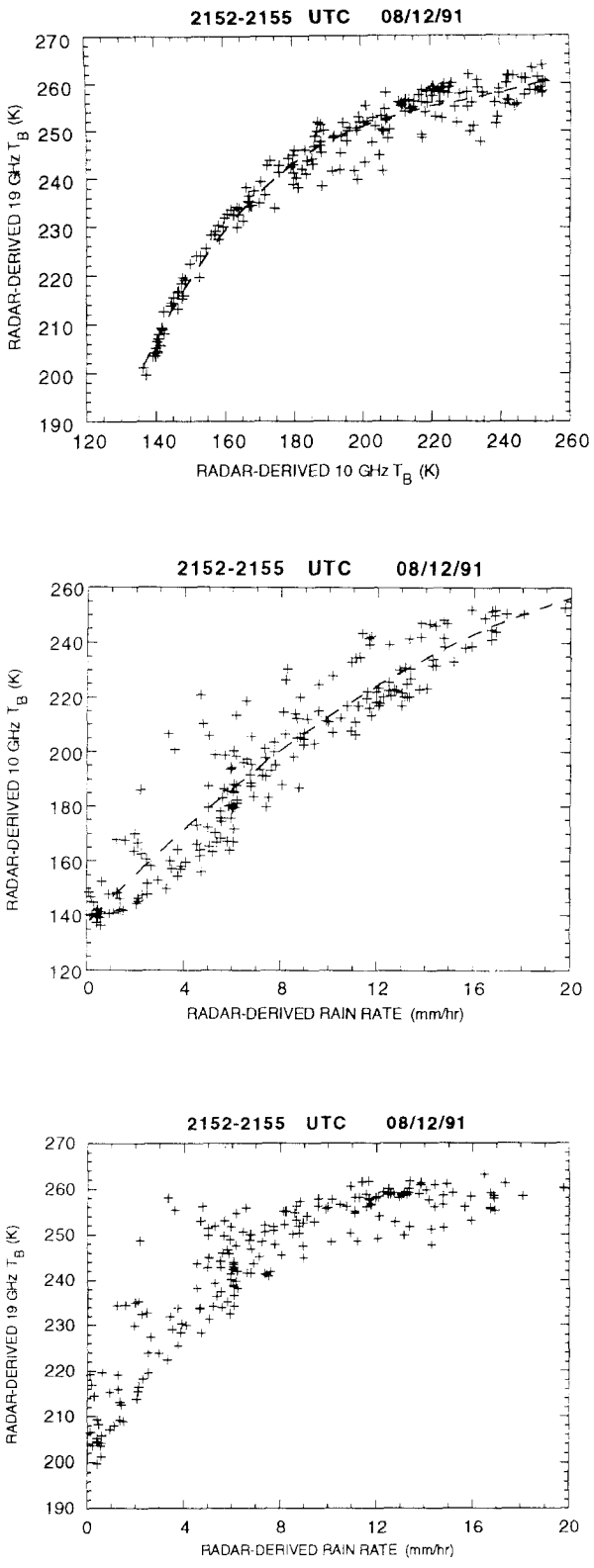


Fig. 13. Behavior of the radar-derived rain rate at 1 km height for the 2152–2155 UTC ocean-based storm. Only the points within $\pm 10$ degrees of nadir are shown. Top: Radar-derived 19 GHz $T_B$ vs. radar-derived 10 GHz $T_B$. Middle: Radar-derived 10 GHz $T_B$ vs. radar-derived rain rate. Bottom: Radar-derived 19 GHz $T_B$ vs. radar-derived rain rate

plotted in the middle and bottom of Fig. 13, respectively. For reasons stated above, scattering effects can be consequential at 19 GHz, and the 19 GHz $T_B$ shows signs of saturation beyond the 10–12 mm hr$^{-1}$ rainfall rate level. This is in accord with the cloud modeling efforts of Adler et al. (1991). At 10 GHz, the $T_B$ shows no sign of saturation for rainfall rates up to 20 mm hr$^{-1}$, although the lack of contrast between the cool ocean and the weak emission from rain rates $<2$ mm hr$^{-1}$ is slightly evident. At these resolutions, the 10 GHz channel appears to be the best overall choice for rain rates below 20 mm hr$^{-1}$. For viewing angles away from nadir, an ocean surface is partially polarized, and the gradual disappearance of the polarization difference as the rain rate increases can identify the onset of light rain (Spencer et al., 1989).

The land-based $T_B$ modeling of Section 5.1 demonstrated that of the four AMPR channels, the 37 GHz $T_B$ came the closest to exhibiting something resembling a trend between columnar mixture water path (MWP) and $T_B$. While it was not our intent to establish a relationship between the two, it is useful from a retrieval standpoint to identify the frequency which best senses the presence of a mixed phase. For this ocean-based case, the 19 GHz channel appears to be the best indicator of the presence of mixed phase, although the $T_B$ saturated beyond a MWP $>0.5$ kg m$^{-2}$ (not shown). The 10 GHz channel, being essentially transparent to the smaller amounts of IWP here, is uncoupled from much of a connection to the MWP.

With regards to the columnar integrated ice water path (IWP) (Fig. 14), the quantities are much less than noted for the land-based situation. As then, the presence of cloud water amongst the lower ice regions warms the overall 85 GHz $T_B$ as a function of the overall ice water path, with scatter increasing proportionately. The trend towards and below 0 K that was noted amongst the 37–85 GHz AMPR $T_B$ difference in Section 5.1 is difficult to discern for this ocean-based storm. In the middle panel of Fig. 14, the AMPR 37–85 GHz difference does seem to level off past a total IWP of $\approx 3$ kg m$^{-2}$, a cutoff value which was also noted in a recent theoretical study (Vivekandandan et al., 1991). The top and bottom panels of Fig. 14 demonstrate that both the 85 GHz $T_B$ and the 37–85 GHz $T_B$ difference are good indicators of

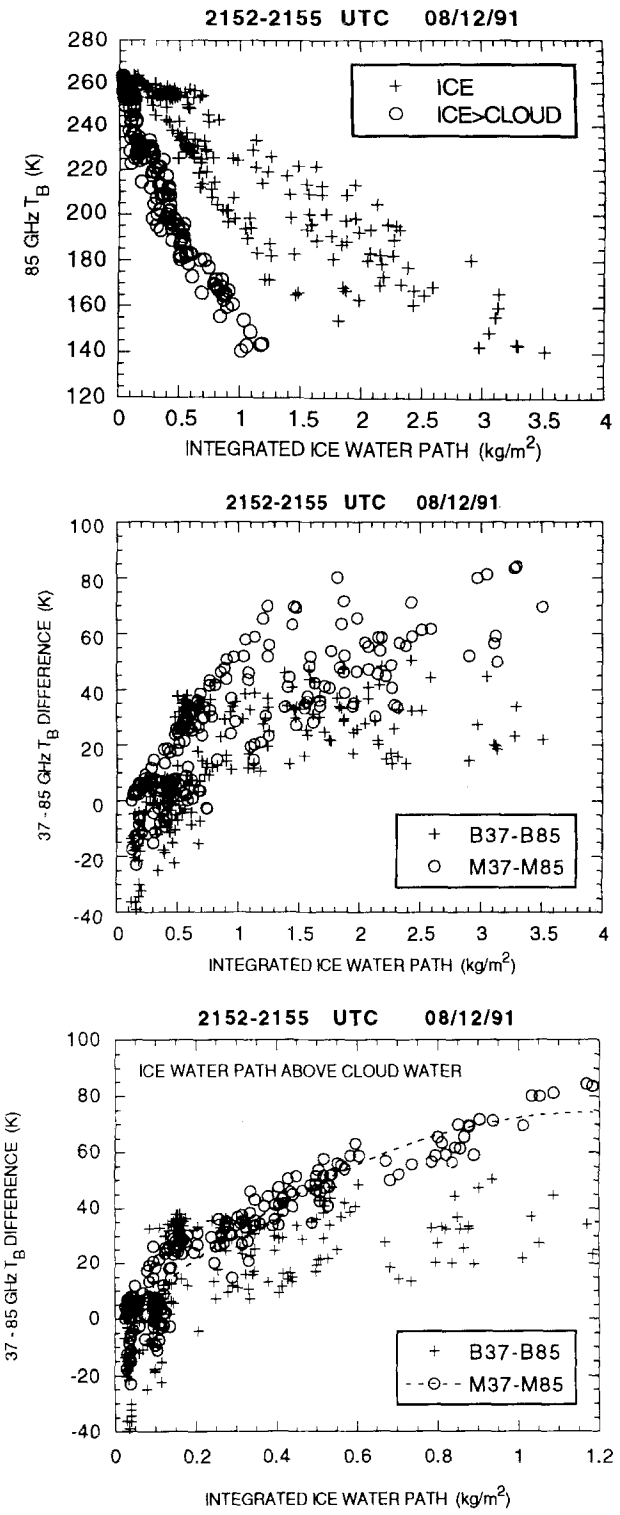


Fig. 14. Behavior of the columnar integrated ice water path (IWP) for the 2152–2155 UTC land-based storm. The format is the same as for Fig. 10

the portion of IWP lying above the cloud water. The bottom panel is somewhat peculiar, as such a tight relationship for the model points (plotted as circles) was not noted in the previous land-based case. As the 19 GHz channel was noted to be the channel which demonstrated some degree of sensitivity to the MWP, this leaves the higher 37 and 85 GHz channels available to sense primarily regions of ice. This is opposed to the land-based case, where the 37 GHz channel was determined to be the MWP indicator. Hence detection of IWP using the 37–85 GHz $T_B$ difference will be biased by the presence of a mixed phase.

### *5.3 Radiative Effects of Cloud LWC Amount and Location*

Inspection of the radar-derived $T_B$ imagery from 2059–2103 UTC (Fig. 2) shows a wide variability in warming and cooling against the AMPR-measured $T_B$. For comparative purposes, a constant cloud LWC profile was used throughout the cloud for radiative transfer modeling whenever the CP-2 $Z_H$ exceeded 5 dBZ. The line traces in Fig. 9 show that at 85 GHz, the radar-derived $T_B$ was up to 80 K cooler than the AMPR $T_B$ over the core region, and up to 40 K warmer over the surrounding region. Oddly enough, at 37 GHz the radar-derived $T_B$ was in close accord with the AMPR $T_B$ over the core and warmer away from the core. For the region surrounding the core, the $T_B$ warming probably results from an overestimate of the cloud water content and a placement too high up in the cloud (peaking at $-10\,^{\circ}$C). For the core region, both this and the likelihood of an overestimate of the ice mass content are suspect, but in some combined fashion that is not very obvious.

To model the core region in depth, the pixel points overlying the immediate core region were isolated (77 points total), and various cloud LWC profiles were superimposed on the associated radar hydrometeor profiles, just as done in Section 5.1. As before, the cloud LWC profiles are defined by the position and temperature of the maximum cloud LWC according to Eq. 13. In Fig. 15, peak cloud LWC $M_0$ of 0.5 and 1.0 g m$^{-3}$ at temperatures $T_0$ of $-5\,^{\circ}$C and $-20\,^{\circ}$C, respectively, are examined for their relative impact upon the 37 and 85 GHz $T_B$ (upper right and middle left). For comparisons sake, the scatter plot in the upper left of Fig. 15 represents the AMPR-observed 85 GHz $T_B$ vs. 37 GHz $T_B$. Note that these points are clumped together near 120 K with most of them lying above the 1:1 line (points where

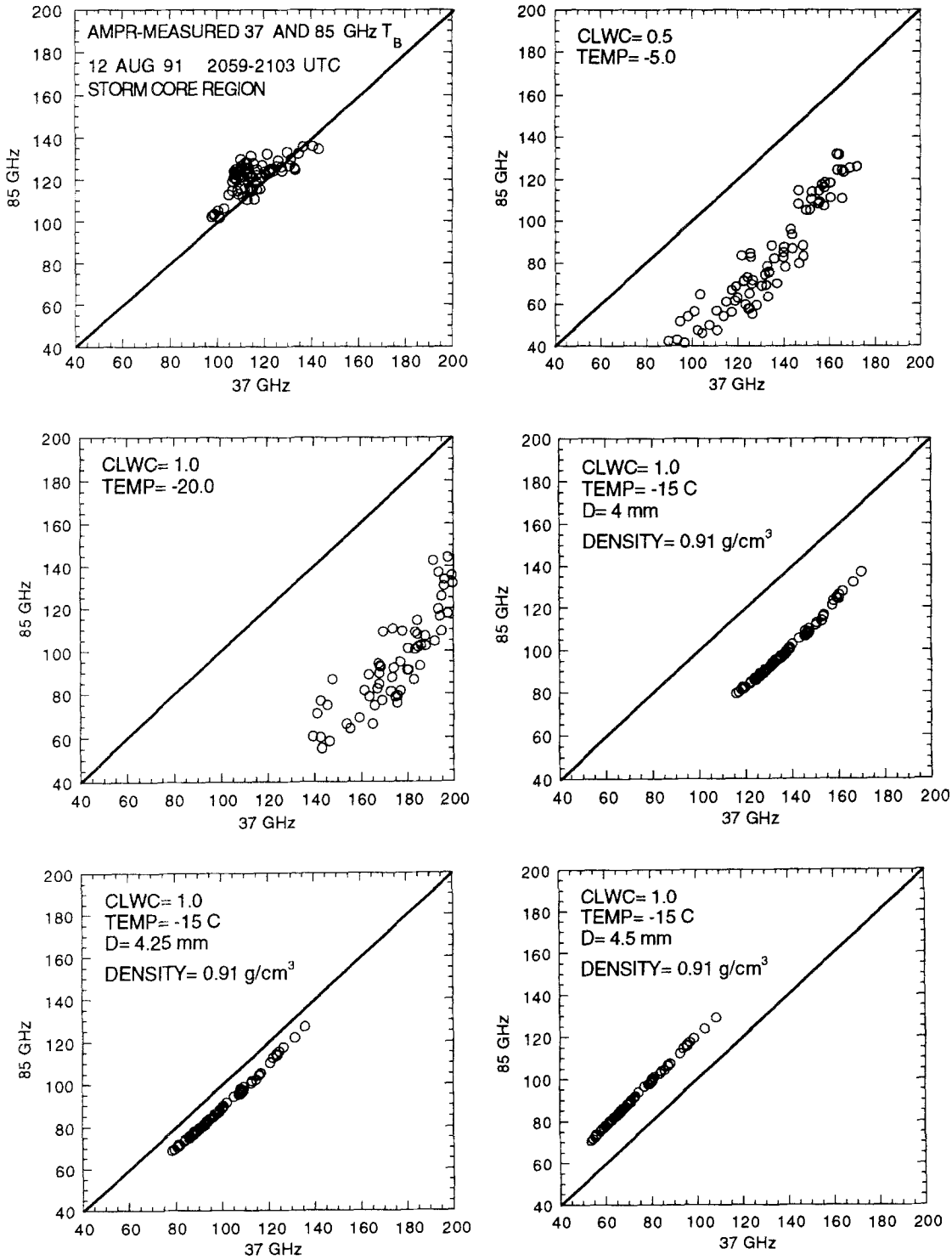


Fig. 15. Scatter plots of 85 GHz vs. 37 GHz $T_B$ for the points encompassing the storm core region for the 2059–2103 UTC flight interval. Top left: AMPR measured $T_B$. Top right: Radar-derived $T_B$ including a cloud liquid water content (CLWC) profile centered at $-5\,°C$ with a peak value of $0.5\,g\,m^{-3}$. Middle left: Same as top right except CLWC profile is centered at $-20\,°C$ with a peak value of $1\,g\,m^{-3}$. Middle right: Radar-derived $T_B$ including a CLWC profile centered at $-15\,°C$ with a peak value of $1\,g\,m^{-3}$, where the ice size distribution has been converted from gamma to monodisperse with a diameter of 4 mm and density of $0.91\,g\,cm^{-3}$. The number density was computed to maintain equivalence with the ice mass content. Lower left: Same as middle right except diameter is 4.25 mm. Lower right: Same as middle right except diameter is 4.5 mm

37 GHz $T_B$ < 85 GHz $T_B$) The net effect of lowering the temperature of maximum CLWC ($T_0$) is to displace each point towards the upper right of the figure (upper right and middle left of Fig. 15). For the points corresponding to the very coldest 85 GHz $T_B$, the 37 GHz $T_B$ warms by 7 K for each 5 K decrease in $T_0$, and 85 GHz $T_B$ is relatively unaffected. This is a manifestation of the 85 GHz $T_B$ saturation referred to in Section 5.1. For points corresponding to the somewhat warmer 37 and 85 GHz AMPR $T_B$, the $T_B$ warm by 5 and 3 K, respectively, for each 5 K decrease in $T_0$. However, unlike the AMPR points, the model points remain relatively spread out in their $T_B$ values, and nowhere does the 37 GHz $T_B$ come close to approaching that at 85 GHz. This suggests that cloud LWC variablities in the core region may be necessary but not sufficient to describe the observed AMPR $T_B$. These results also suggest that subtle size distribution effects may be present in the core region.

### 5.4 *Radiative Effects of Ice Particle Size*

To explain the 37 GHz $T_B$ < 85 GHz $T_B$ behavior noted over the core region by means other than the vertical CLWC profile, we next examine the effect of ice particle size. An earlier publication by Vivekanandan et al. (1993) demonstrated that it is possible to obtain 37 GHz $T_B$ < 85 GHz $T_B$ when a dominant ice particle size is present. At AMPR frequencies, the ice dielectric constant is relatively unaffected by frequency, so for a given size, the net effect of increasing frequency is to translate into the resonance region of the Mie extinction curve. For certain sizes, it is possible for the extinction cross section to be larger at the smaller of two frequencies. A plot of the extinction coefficient in units of $km^{-1}$ vs. ice radius is plotted in Fig. 16. The ice mass content $M_i$ is kept constant at 1 $g\,m^{-3}$ for a monodisperse (single size) distribution of densities $\rho = 0.60$ and 0.91 $g\,cm^{-3}$. The remaining free size distribution parameter is the number concentration $N$, given by

$$N = (6000/\pi\rho D^3)M_i \quad m^{-3} \tag{14}$$

where $D$ is the particle diameter in mm, $M_i$ is the ice mass content in $g\,m^{-3}$, and $\rho$ is the ice density in $g\,cm^{-3}$. At 10 GHz, Mie effects are slight and the extinction curve rises smoothly. The transition radius between 37 and 85 GHz occurs at 2.2 and

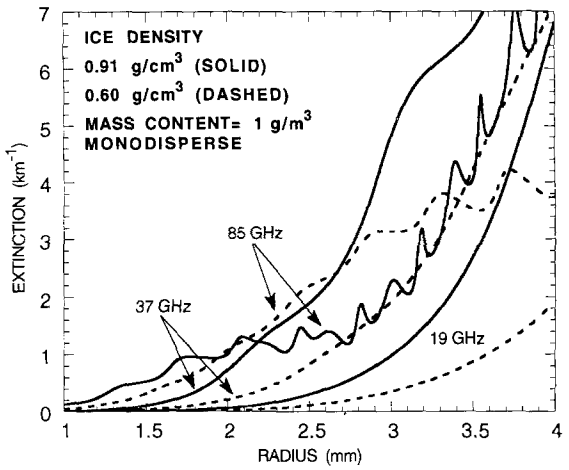


Fig. 16 Behavior of the 19, 37, and 85 GHz extinction coefficient for a 1 $g\,m^{-3}$ monodisperse (single size) ice size distribution of density 0.60 (dashed line) and 0.91 (solid line) $g\,cm^{-3}$

3.4 mm radius for the 0.91 and 0.60 densities, respectively. It is possible that an ice size distribution that is narrowly centered about these dominant sizes could preferentially enhance the overall scattering of the upwelling emission from the rain and mixture region at 37 GHz. Although we have no means to verify the particle size in the convective core, it is worthwhile to note that other scientists have used similar arguments to explain polarimetric radar and radiometric anomalies. Zrnic et al. (1993) hypothesized that large wet aggregates of $\approx$10 mm diameter were responsible for a change in sign of the radar differential propagation phase $K_{DP}$ throughout the melting band of a mesoscale convective system. Fulton and Heymsfield (1991) surmised that hail sizes between 10–15 mm diameter were responsible for high DFR-hail signal values noted at 5–6 km height in Alabama convection. Gasiewski (1992) demonstrated that a series of microwave channels in the 90–400 GHz range would be able to detect the frequency at which the hydrometeor extinction displays minimum sensitivity to the mean particle size. Near this frequency, the slope of the brightness spectrum can be related to the mean particle size.

To test this hypothesis, the radar-derived ice gamma distributions of Section 5 were replaced with their mass-equivalent monodisperse counterparts (this replacement does not conserve the observed radar reflectivity). Particle diameters of 4, 4.25 and 4.5 mm and density 0.91 $g\,cm^{-3}$ were tested. The results are plotted in the middle right and lower two panels of Fig. 15, and demonstrate

the $T_B$ perturbation effect quite strikingly. In all three cases, the 37 and 85 GHz $T_B$ are nearly linearly related with a slope near unity, with a 37–85 GHz $T_B$ offset of +45, +12, and −13 K for diameters of 4, 4.25 and 4.5 mm, respectively. This suggests that the ice particles in the upper reaches of cloud may be narrowly distributed around a common size between 4 to 4.5 mm diameter. Judging by the vertical extent of the high reflectivity column (Fig. 3), it is possible that the strong vertical air motion lofted large high density hail up into and amongst the lower density, more widely distributed in size, but smaller ice crystals and aggregates in upper regions between 10–13 km height. Although nadir-viewing 92 GHz $T_B$ measurements below 100 K were reported during the 1986 COHMEX measurements, the differing view angles of the 37 and 85 GHz channels never viewed along a common path along nadir into the storm core. The 37 GHz channel peered 45° ahead and intercepted the lower density graupel which produces a more moderate $T_B$. We offer this scenario as a possible explanation of the AMPR $T_B$ over strong storm cores, and suggest that this $T_B$ feature is an indicator of the strength of the vertical air motion within the storm core. As mentioned, the techniques proposed by Gasiewski (1992) for channels up to 340 GHz hold promise for detection of even smaller particles commonly found in cloud and ice regions. Similar $T_B$ anomalies might be noted amongst high frequency channels between 90 and 340 GHz when overflying regions where certain ice and cloud particle sizes dominate.

## 6. Conclusions

The sensitivity of the Advanced Microwave Precipitation Radiometer to both land and oceanbased precipitating storms has been demonstrated for typical summer Florida convective storms. The fine resolution radiative effects are quite different than radiative effects observed at the same frequencies by radiometers with coarser resolutions. The scanning capability of the AMPR revealed subtle cloud characteristics that would go undetected to coarser resolution observations. Data from the NCAR CP-2 multiparameter radar was remapped into a geometry which enabled direct comparison with the multichannel AMPR imagery. For example, the correlation between the 10 km height radar reflectivity $Z_H$ and the 85 GHz AMPR $T_B$ image was very strong for both the land and ocean storms.

A extrapolation-based inversion algorithm was applied to the CP-2 radar data corresponding to the AMPR imagery location. The differential reflectivity $Z_{DR}$ was used in a qualitative fashion to determine if a mixture of rain and ice was present. Since drop size distribution (DSD) parameters and relations are better established for rain than for ice, the method gradually extrapolated the gamma DSD parameters from the rain upwards into the ice, using the observed radar reflectivity $Z_H$ as a direction guide for the extrapolation of the DSD parameters. The result is a non-unique DSD which is numerically consistent with the observed radar $Z_H$, and which reduced to the exponential case for $Z_H$ below 35 dBZ. Two storms were modeled from the 12 August 1991 ER-2 flights during CaPE, a land-based storm during the 2059–2103 UTC flight segment, and an ocean-based storm from 2152–2155 UTC. For the land-based storm, integrated columnar ice water contents exceeding 20 kg m$^{-2}$ were derived from radar, while columnar mixture and rain contents peaked near 7 kg m$^{-2}$. For the ocean-based storm, the associated columnar values were much less, peaking near 3.5 kg m$^{-2}$. Maximum radar-derived rainfall rates for the land and ocean storms were found to be 60 and 18 mm hr$^{-1}$, respectively.

Radiative transfer modeling using the radar-derived DSD profiles was performed for both the land and ocean based storms. Although the entire AMPR image was modeled for comparative purposes, due to the limitations of plane parallel modeling, only the points within ±10° about nadir were extracted for retrieval purposes. Radar-derived 85 GHz $T_B$ showed signs of saturation at 50 K beyond total columnar ice water path (IWP) values of 20 kg m$^{-2}$, while at the same time the AMPR 37–85 GHz $T_B$ difference fell near or below zero for IWP values exceeding 5 kg m$^{-2}$. This trend towards zero could not be duplicated by the gamma ice distributions here nor with variable amounts of cloud liquid water throughout the core region. However, the IWP existing above the region of cloud liquid water followed the 85 GHz $T_B$ quite tightly with minimal scatter amongst the points.

Since many previous studies have not considered or questioned the presence of a mixed phase in the

radiative transfer models, the radar-derived $T_B$ were examined for the channel which displayed the best statistical correlation with the overall columnar mixture water path (MWP). For the land and ocean storms sampled here, the 37 and 19 Ghz channels were noted to be the best indicators in this regard, respectively. Mixtures of ice and rain will impact IWP retrieval algorithms that use 37 and 19 GHz channels as their dependent parameters. Over ocean, the 19 GHz channel was noted to saturate near 260 K for rain rates beyond 10 mm $hr^{-1}$, while the 10 GHz channel demonstrated dynamic range for the highest rain rates observed here near 20 mm $hr^{-1}$. Over land, although peak rain rates approached 60 mm $hr^{-1}$, the 85 and 37 GHz $T_B$ depressions in these regions were more closely tied to increases in the IWP and MWP, respectively. Overall, the modeling results tend to confirm the belief that a multispectral, vertical profiling type of precipitation retrieval algorithm is ultimately necessary to interpret passive radiometric observations from space (Smith et al., 1992; Mugnai et al., 1993).

By shifting the location and peak amount of the cloud liquid water profile, the impact of coexisting cloud water and ice was examined. Under conditions where the 85 GHz $T_B$ had not yet saturated below 150 K, the $T_B$ warmed by 5 and 3 K at 37 and 85 GHz, respectively, for each 5 K decrease in the location of the peak cloud water temperature. A size-sorting phenomenon is proposed as a explanation to the odd $T_B$ behavior over the storm core regions where 85 GHz $T_B < 120$ K and the 37–85 GHz $T_B$ difference approached zero. Since the ER-2 flew along a track where the AMPR nadir view was directly down into the storm core, both 37 and 85 GHz channels sensed regions in the upper cloud levels, where extended vertical radar reflectivity columns were present due to vertical air motion. Radiative transfer results demonstrated that the presence of ice particle sizes near 4.5 mm diameter and of density 0.91 g $cm^{-3}$ (somewhat larger for lower density ice) could duplicate this type of $T_B$ behavior.

On a final note, the recent TOGA-COARE field experiment in the South Pacific Ocean included ER-2-based measurements taken with the AMPR and the Multifrequency Imaging Radiometer (MIR), a nine-channel radiometer designed to operate between 89 and 325 GHz (Racette et al., 1992). The ER-2-based multispectral measurements from CaPE and TOGA-COARE will play a major role in determining the future requirements for high resolution passive microwave imagery from space.

**Acknowledgments**

Two of the authors (JT and JV) acknowledge support from NASA Earth Science and Applications Division grant NAG8-645. We thank John Lutz and the NCAR radar staff for their efforts in transporting, installing, and maintaining the CP-2 radar during CaPE. The Cartesian radar data format was developed for workstation applications by Bill Anderson and L. Jay Miller of NCAR/MMM. Computational support was provided by the NCAR Scientific Computing Division. Ms. V. L. Griffin of NASA/MSFC assisted with coordinaton of the ER-2 flights during CaPE. The authors acknowledge the efforts and encouragement of Alberto Mugnai of the Consiglio Nazionale dell Richerche in Frascati, Italy, and Eric Smith of Florida State University in coordinating each others respective research efforts in a cooperative fashion.

**References**

Adler, R. F., Mack, R. A., Prasad, N., Yeh, H.-Y. M., Hakkarinen, I. M., 1990: Aircraft microwave observations and simulations of deep convection from 18 to 183 GHz. Part I: Observations. *J. Atmos. Oceanic Technol.* **7**, 377–391.

Adler, R. F., Yeh, H.-Y. M., Prasad, N., Tao, W.-K., Simpson, J., 1991: Microwave simulations of a tropical rainfall system with a three-dimensional cloud model. *J. Appl. Meteor.*, **30**, 924–953.

Balakrishnan, N., Zrnic, D. S., 1990: Estimation of rain and hail rates in mixed-phase precipitation. *J. Atmos. Sci.*, **47**, 565–583.

Bringi, V. N., Vivekanandan, J., Tuttle, J. D., 1986: Multiparameter radar studies in Colorado convective storms. Part 2: Hail detection studies. *J. Atmos. Sci.*, **43**, 2564–2577.

Bringi, V. N., Hendry, A., 1990: Technology of polarization diversity radars for meteorology. Chapter 19a. In: Altas, D. (ed.) *Radar in Meteorology*. Boston: AMS, pp. 153–190.

Chandrasekar, V., Atwater, C. A., Vonder Haar, T. H., 1991: Convective latent heating estimates from radar data. *Proc. 1991 AMS Radar Conference*, Paris, pp. 155–158.

Evans, K. F., Vivekanandan, J., 1990: Multiparameter radar and microwave radiative transfer modeling of nonspherical atmospheric ice particles. *IEEE Trans. Geosci. Remote Sensing*, **28**, 423–437.

Evans, K. F., Stephens, G. L., 1991: A new polarized atmospheric radiative transfer model. *J. Quant. Spectrosc. Radiat. Trans.*, **46**, 413–423.

Fulton, R., Heymsfield, G. M., 1991: Microphysical and radiative characteristics of convective clouds during COHMEX. *J. Appl. Meteor.*, **30**, 98–116.

Gasiewski, A. J., Kunkee, D. B., 1992: Laboratory demonstration of electronic polarization basis rotation. *Proc. IEEE MTT-S Int. Microwave Symp.*, Albuquerque, NM.

Gasiewski, A. J., 1992: Numerical sensitivity analysis of passive EHF and SMMW channels to tropospheric water vapor, clouds, and precipitation. *IEEE Trans. Geosci. Remote Sensing*, **30**, 859–870.

Grody, N. C., 1991: Classification of snow cover and precipitation using the Special Sensor Microwave Imager. *J. Geophys. Res.*, **96**, D4, 7423–7435.

Hakkarinen, I. M., Adler, R. F., 1988: Observations of precipitating convective systems at 92 and 183 GHz: Aircraft results. *Meteorol. Atmos. Phys.*, **38**, 164–182.

Herzegh, P. H., Jameson, A. R., 1992: Observing precipitation through dual-polarization radar measurements. *Bull. Amer. Meteor. Soc.*, **73**, 1365–1374.

Jameson, A. R., 1991: The effect of drop size distribution variability on radiometric estimates of rainfall rates for frequencies from 3 to 10 GHz. *J. Appl. Meteor.*, **30**, 1025–1033.

Kattawar, G. W., Hitzfelder, S. J., Binstock, J., 1973: An explicit form of the Mie phase matrix for multiple scattering calculations in the $I, Q, U, V$ representation. *J. Atmos. Sci.*, **30**, 289–295

Kummerow, C., Hakkarinen, I., Pierce, H. F., Weinman, J. A., 1991: Determination of precipitation profiles from airborne passive microwave radiometric measurements. *J. Atmos. Oceanic Technol.*, **8**, 148–158.

Liebe, H. J., 1985: An updated model for millimeter wave propagation in moist air. *Radio Science*, **20**, 1069–1089.

Liu, S., Curry, J. A., 1992: Retrieval of precipitation from satellite microwave measurement using both emission and scattering. *J. Geophys. Res.*, **97**, D9, 9959–9974.

Marshall, J. S., Gunn, K. L. S., 1952: Measurement of snow parameters by radar. *J. Meteor.*, **9**, 322–327.

Mugnai, A., Cooper, H. J., Smith, E. A., Tripoli, G. J., 1990: Simulation of microwave brightness temperatures of an evolving hail storm at SSM/I frequencies. *Bull. Amer. Meteor. Soc.*, **71**, 2–13.

Mugnai, A., Smith, E. A., Tripoli, G. J., 1993: Foundations for statistical-physical precipitation retrieval from passive microwave satellite measurements. Part II: Emission source and generalized weighting function properties of a time dependent cloud-radiation model. *J. Appl. Meteor.*, **32**, 17–39.

Prabhakara, C., Dalu, G., Liberti, G. L., Nucciarone, J. J., Suhasini, R., 1992: Rainfall estimation over oceans from SMMR and SSM/I microwave data. *J. Appl. Meteor.*, **31**, 532–552.

Racette, P. E., Dod, L. R., Shiue, J. C., Adler, R. F., Jackson, D. M., Gasiewski, A. J., Zacharias, D. S., 1992: Millimeter wave imaging radiometer for cloud, precipitation, and atmospheric water vapor studies. *Proc. IGARSS-92*, Houston, TX, pp. 1426–1428.

Russchenberg, H. W. J., Ligthart, L., 1991: Radar measurements of the dispersion factor of the gamma distribution of raindrops. *Proc. Int. Workshop on Multiparameter Radar Applied to Microwave Propagation*, Graz, Austria, pp. 141–147.

Sachidananda, M., Zrnic, D. S., 1986: Differential propagation phase shift and rainfall rate estimation. *Radio Science*, **21**, 235–247.

Simpson, J., Adler, R. F., North, G., 1988: A Proposed Tropical Rainfall Measuring Mission (TRMM) satellite. *Bull. Amer. Meteor. Soc.*, **69**, 278–295.

Smith, E. A., Mugnai, A., Cooper, H. J., Tripoli, G. J., Xiang, X., 1992: Foundations for statistical-physical precipitation retrieval from passive microwave satellite measurements. Part I: Brightness temperature properties of a time-dependent cloud-radiation model. *J. Appl. Meteor.*, **31**, 506–531.

Smith, E. A., Xiang, X., Mugnai, A., Hood, R. E., Spencer, R. W., 1993: High resolution microwave imaging of the Earth with the Advanced Microwave Precipitation Radiometer. Part II: Implications of high resolution measurements with a 10.7 GHz channel on precipitation retrieval. *J. Atmos. Oceanic Technol.*, (in press).

Smith, P. L., 1984: Equivalent radar reflectivity factors for snow and ice particles. *J. Climate Appl. Meteor.*, **23**, 1258–1260.

Spencer, R. W., Goodman, H. M., Hood, R. E., 1989: Precipitation retrieval over land and ocean with the SSM/I: Identification and characteristics of the scattering signal. *J. Atmos. Oceanic Technol.*, **6**, 254–273.

Spencer, R. W., Hood, R. E., LaFontaine, F., Smith, E. A., 1993: High resolution microwave imaging of the Earth with the Adanced Microwave Precipitation Radiometer. Part I: System description and sample imagery. *J. Atmos. Oceanic Technol.*, (in press).

Ulbrich, C. W., 1983: Natural variations in the analytical form of the raindrop size distribution. *J. Climate Appl. Meteor.*, **22**, 1764–1775.

Vivekanandan, J., Turk, J., Stephens, G. L., Bringi, V. N., 1990: Microwave radiative transfer studies using combined multiparameter radar and radiometer measurements during COHMEX. *J. Appl. Meteor*, **29**, 561–585.

Vivekanandan, J., Turk, J., Bringi, V. N., 1991: Ice water path estimation and characterization using passive microwave radiometry. *J. Appl. Meteor.*, **30**, 1407–1421.

Vivekanandan, J., Raghavan, R., Bringi, V. N., 1992: Polarimetric radar modeling of mixtures of precipitation particles. *IEEE Trans. Geosci. Remote Sensing*, **31**, 1017–1030.

Vivekanandan, J., Turk, J., Bringi, V. N., 1993: Advanced Microwave Precipitation Radiometer (AMPR) and multiparameter radar comparisons of precipitation. *IEEE Trans. Geosci. Remote Sensing*, **31**, 860–870.

Yeh, H.-Y. M., Prasad, N., Mack, R. A., Adler, R. F., 1990: Aircraft microwave observations and simulations of deep convection from 18 to 183 GHz. Part II: Model results. *J. Atmos. Oceanic Technol.*, **7**, 392–410.

Zrnic, D. S., Balakrishnan, N., Ziegler, C. L., Bringi, V. N., Aydin, K., Matejka, T., 1993: Polarimetric signatures in the stratiform region of a mesoscale convective system. *J. Appl. Meteor.*, **32**, 678–693.

Authors' addresses: J. Turk, Department of Electrical Engineering, Colorado State University, Fort Collins, CO 80523 U.S.A.; J. Vivekanandan, National Center for Atmospheric Research, Research Applications Program, Boulder, CO 80307 U.S.A.; F. S. Marzano, Dipartimento die Ingegneria Elettronica, Università di Roma "La Sapienza", Via Eudossiana 18, I-00184 Rome, Italy; R. E. Hood and R. W. Spencer, National Aeronautics and Space Administration, ES-43, Marshall Space Flight Center, AL 35812, U.S.A.; F. J. LaFontaine, Universities Space Research Association, NASA/Marshall Space Flight Center, Huntsville, AL 35812, U.S.A.